Empirical and theoretical investigation of the noise performance of indirect detection, active matrix flat-panel imagers (AMFPIs) for diagnostic radiology

J. H. Siewerdsen, L. E. Antonuk, Y. El-Mohri, J. Yorkston, W. Huang, and J. M. Boudry
Department of Radiation Oncology, University of Michigan Medical Center, Ann Arbor, Michigan 48109

I. A. Cunningham
Imaging Research Laboratories, The John P. Roberts Research Institute and Department of Diagnostic Radiology, London Health Sciences Centre–Victoria, and The University of Western Ontario, London, Ontario N6A 5K8, Canada

Noise properties of active matrix, flat-panel imagers under conditions relevant to diagnostic radiology are investigated. These studies focus on imagers based upon arrays with pixels incorporating a discrete photodiode coupled to a thin-film transistor, both fabricated from hydrogenated amorphous silicon. These optically sensitive arrays are operated with an overlying x-ray converter to allow indirect detection of incident x rays. External electronics, including gate driver circuits and preamplification circuits, are also required to operate the arrays. A theoretical model describing the signal and noise transfer properties of the imagers under conditions relevant to diagnostic radiography, fluoroscopy, and mammography is developed. This frequency-dependent model is based upon a cascaded systems analysis wherein the imager is conceptually divided into a series of stages having intrinsic gain and spreading properties. Predictions from the model are compared with x-ray sensitivity and noise measurements obtained from individual pixels from an imager with a pixel format of 1536×1920 pixels at a pixel pitch of 127 μm. The model is shown to be in excellent agreement with measurements obtained with diagnostic x rays using various phosphor screens. The model is used to explore the potential performance of existing and hypothetical imagers for application in radiography, fluoroscopy, and mammography as a function of exposure, additive noise, and fill factor. These theoretical predictions suggest that imagers of this general design incorporating a CsI:Tl intensifying screen can be optimized to provide detective quantum efficiency (DQE) superior to existing screen-film and storage phosphor systems for general radiography and mammography. For fluoroscopy, the model predicts that with further optimization of a-Si:H imagers, DQE performance approaching that of the best x-ray image intensifier systems may be possible. The results of this analysis suggest strategies for future improvements of this imaging technology. © *1997 American Association of Physicists in Medicine.* [S0094-2405(97)01401-6]

Key words: digital x-ray imaging, active matrix flat-panel imager, amorphous silicon, quantum accounting diagram, detective quantum efficiency

I. INTRODUCTION

Detailed knowledge of the noise performance of an x-ray imaging system is a crucial element in understanding the limitations of the system. Such an understanding is particularly valuable during the initial development of a new technology, since it can aid in the challenging task of system optimization. Active matrix, flat-panel imagers (AMFPIs) are a new, rapidly developing x-ray imaging technology which could benefit from such insight. In this paper, we report a theoretical and empirical investigation of the noise performance of a particular class of AMFPIs-those employing an array with pixels consisting of a hydrogenated amorphous silicon (a-Si:H) thin-film transistor (TFT) coupled to an a-Si:H photodiode sensor. In such imagers, the optically sensitive array detects the x rays indirectly by means of an overlying material, such as a phosphor or scintillator, which converts incident x rays to optical photons. External electronics control the readout and processing of analog signals from the array.

Previously and in the context of fluoroscopic imaging, Schiebel *et al.*[1] have published a spatial frequency-dependent analysis of the signal and noise performance of a small AMFPI of similar design based on a 200 μm pitch, 192×192 pixel array ($\sim 3.8 \times 3.8$ cm^2). In addition, Chabbal *et al.*[2] have shown empirical, spatial frequency-dependent signal and noise measurements for an a-Si:H AMFPI incorporating a single diode switching element. Ross *et al.*[3] have reported a theoretical analysis of the noise performance of an imager based on the same general array design in the context of x-ray diffraction for protein crystallography. Finally, a theoretical examination of the frequency-independent signal and noise performance of direct-detection AMFPIs utilizing an array with TFTs coupled to a thick amorphous–selenium

layer has been published by Zhao *et al.*[4] The present paper focuses on the development of a general theoretical signal and noise model for indirect-detection, TFT+photodiode AMFPIs. This model is spatial frequency-dependent and is based upon a serial cascaded systems approach in which the imaging system is conceptually divided into a number of discrete stages. Each stage represents a physical process having intrinsic signal and noise transfer properties. The power in such an approach is that it allows an examination of the performance of not only the entire system, but also any subset of the imaging chain. This provides a tool for identifying the individual stages which limit system performance and a guide for optimization of the entire system.

The model is based upon both a theoretical and empirical knowledge of the various stages in the imaging chain. In this paper, a brief background description of cascaded systems analysis in the context of modeling the imaging properties of *a*-Si:H AMFPIs is given. In Sec. III the stages comprising the imaging chain are discussed with emphasis on processes associated with the imaging array, and expressions for the signal and noise properties are derived. A partial confirmation of the validity of the analysis is provided by comparison of model predictions with x-ray sensitivity and noise measurements from individual pixels obtained from an imager utilizing a large-area, high-resolution array.[5] Experimental determination of the frequency-dependent noise power spectrum is beyond the scope of the present paper. Rather, the present paper is restricted to a description of the presampling signal and noise properties of individual pixels, and characteristics which depend upon the sampling matrix are not discussed. Finally the model is used to explore the potential performance of TFT+photodiode AMFPIs for various applications in diagnostic x-ray imaging and under different modes of operation. The detective quantum efficiency (DQE) for imagers in the context of diagnostic radiography, fluoroscopy, and mammography is calculated as a function of a variety of system and irradiation conditions, and comparisons are made with existing imaging technologies. Strategies for future optimization of *a*-Si:H imaging systems and extension of this formalism to other AMFPI designs are discussed.

II. BACKGROUND

A. Cascaded linear systems analysis

A cascaded linear systems model is used to model the signal and noise performance of *a*-Si:H imagers because of the simplicity and physical intuitiveness of such an approach. Such analysis has been shown to accurately describe the signal and noise performance of other imaging systems.[6,7] The model requires that the system have a linear (or linearizable) and shift-invariant signal response. In addition, image noise is expressed in terms of the noise power spectrum, which requires that the noise processes be stationary.[8] The effect of nonlinear signal response is discussed in Sec. III B 4, and since discussion in the present manuscript is limited to presampling signal and noise properties, the assumption of shift invariance is appropriate. The presampling signal is the sig-
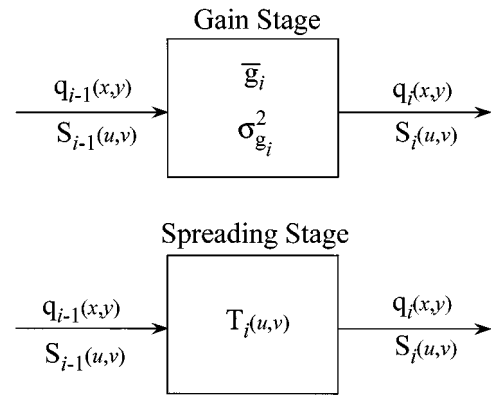

FIG. 1. Schematic illustration of the properties governing the signal and noise transfer for gain and spreading stages.

nal which, if evaluated (i.e., sampled) at positions corresponding to the centers of each detector element, gives the correct values for each element. Furthermore, the system is assumed ergodic (and therefore stationary[8]), so that the individual pixel noise may be determined from either an ensemble of pixels or from a single pixel measured repeatedly.

The cascaded systems approach represents the imaging system as a series of discrete stages, where each stage represents either a quantum gain or spatial spreading (blurring) process. Each of these processes has signal and noise transfer characteristics as described by Rabbani *et al.*[9] with the relationship between the input and output signal and noise governed by the properties summarized in Fig. 1. For each stage, i, the signal is described by the distribution of image quanta, $q_i(x,y)$, and the noise is described by the noise power spectrum (NPS), $S_i(u,v)$, where (x,y) and (u,v) are orthogonal spatial and spatial-frequency coordinates, respectively. A process which changes the mean number of image quanta is described by a gain stage and characterized by an intrinsic average gain, $\bar{g}_i$, and a variance in that gain, $\sigma_{g_i}^2$. A process which changes the spatial distribution of the image quanta is described by a spreading stage and characterized by the modulation transfer function (MTF), $T_i(u,v)$, given by the modulus of the Hankel transform of the point spread function[10] (PSF), $p_i(x,y)$. The NPS associated with additive noise sources is represented by $S_{add}(u,v)$. The entire system is represented as a serial cascade of such gain and spreading stages, where the output of one stage provides the input to the subsequent stage. This analysis requires that each stage represent either a gain or a spreading process,[9,11] and the order of the stages must reflect the physical imaging system. If the gain, noise, and spreading properties of each stage are known, then the performance of the entire system may be deduced.

B. Signal transfer properties of gain and spreading stages

The signal transfer properties of a stage determine how the distribution of image quanta, $q_i(x,y)$, is transferred to the

output of the stage. For a gain stage, the mean fluence of output quanta, $\bar{q}_i$, is directly related to the mean fluence of input quanta, $\bar{q}_{i-1}$, by the mean gain, $\bar{g}_i$,

$$\bar{q}_i = \bar{g}_i \bar{q}_{i-1} \quad \text{(gain stage)}. \tag{1a}$$

A stochastic spreading stage changes the spatial distribution of the image quanta by randomly displacing each quantum by a distance with probability described by the normalized PSF,

$$q_i(x,y) = q_{i-1}(x,y) **_s p_i(x,y)$$

$$\text{(stochastic spreading stage)}, \tag{1b}$$

where $**_s$ represents this two-dimensional stochastic spreading process.[12] It is written in this form for comparison with a (''conventional'') convolution and has been referred to as a ''stochastic'' convolution.[12] Equation (1b) represents the physical process of randomly displacing individual quanta according to a probability described by the PSF. This would occur, for example, when light photons generated in a scintillating phosphor are randomly scattered before reaching the exit surface. By contrast, a spreading stage such as integration of quanta by an aperture is described by a conventional convolution:[12]

$$q_i(x,y) = q_{i-1}(x,y) ** \Pi_i(x/a_x, y/a_y)$$

$$\text{(deterministic spreading stage)}, \tag{1c}$$

where $\Pi_i(x/a_x, y/a_y)$ is a two-dimensional rect function with dimensions corresponding to the width, a_x, and length, a_y, of the sampling aperture. This integration (''counting'') of quanta corresponds to convolution with a rect of unity height and is referred to as a ''deterministic'' spreading stage.

C. Noise transfer properties of gain and spreading stages

The noise transfer properties of a stage determine how the second-order statistics of the distribution of image quanta are transferred to the output. For a gain stage, the average gain and gain-variance determine the noise transfer,[9]

$$S_i(u,v) = \bar{g}_i^2 S_{i-1}(u,v) + \sigma_{g_i}^2 \bar{q}_{i-1} + S_{\text{add}_i}(u,v)$$

$$\text{(gain stage)}. \tag{2a}$$

Note that for an ideal, unity gain stage [$\bar{g}_i = 1$, $\sigma_{g_i}^2 = 0$, and $S_{\text{add}_i}(u,v) = 0$] the NPS is unaffected. It is often convenient to express the gain-variance in terms of the Poisson excess,[11] ϵ_{g_i}, which describes the relative amount by which the gain-variance exceeds that of a Poisson distribution or, alternatively, in terms of the statistical (Swank) factor.[13]

For a stochastic spreading stage, the noise transfer is described by the relation of Rabbani et al.,[9]

$$S_i(u,v) = [S_{i-1}(u,v) - \bar{q}_{i-1}] T_i^2(u,v) + \bar{q}_{i-1}$$

$$\text{(stochastic spreading stage)}. \tag{2b}$$

Equation (2b) indicates that for a stochastic spreading stage, the correlated component of the noise $[S_{i-1}(u,v) - \bar{q}_{i-1}]$ is

modulated by the square of the MTF, whereas the uncorrelated component ($\bar{q}_{i-1}$) is unaffected.[9] For a deterministic spreading stage, the NPS is transferred directly by the square of the MTF,[14]

$$S_i(u,v) = S_{i-1}(u,v) T_i^2(u,v)$$

$$\text{(deterministic spreading stage)}. \tag{2c}$$

Equations (2b) and (2c) indicate that for an ideal spreading stage [$T_i(u,v) = 1$] the NPS is unaffected.

A property exists which is often useful in simplifying the representation of complicated systems involving a number of consecutive binomial selection processes[8] (e.g., stages representing absorption or attenuation). A consecutive series of such stages $(j, j+1, j+2, \ldots, j+n)$ can be equivalently represented as a single stage, i, with mean gain given by a linear combination of the individual gains,

$$\bar{g}_i = \prod_{k=0}^{n} \bar{g}_{j+k} \tag{3a}$$

and gain-variance given by the relation for a binomial process,

$$\sigma_{g_i}^2 = \bar{g}_i(1 - \bar{g}_i). \tag{3b}$$

Furthermore, although it is generally important to have the gain and spreading stages describing the system in a certain order, a special case exists with regard to binomial selection and stochastic spreading stages. The order of such stages may be reversed without affecting the transfer of signal or noise through the imaging chain (i.e., binomial selection and stochastic spreading stages commute[12]).

D. Quantum accounting diagrams

The noise transfer characteristics of imaging systems are strongly influenced by the number of image quanta propagating through each stage. In particular, an insufficient number of quanta can lead to secondary quantum sinks.[11,15] The propagation of image quanta through the cascade of gain and spreading stages representing an imaging system may be plotted schematically in a spatial frequency-dependent quantum accounting diagram (QAD).[11] The QAD plots the running product, $QAD_i(u,v)$, of the gains and squared MTFs at each stage in the system (normalized to unity at stage 0) and is useful both as an intuitive tool to understand the transfer characteristics of the system and as a means of identifying at which stage and at what frequencies quantum sinks occur.

Cascaded systems analysis has been used to model the performance of a number of x-ray imaging systems. Cunningham et al.[11] and Westmore et al.[16] discussed the technique in relation to a hypothetical system composed of a change-coupled device (CCD) camera and a luminescent phosphor. Spekowius et al.[7] applied similar formalism in describing the transfer characteristics of an x-ray image intensifier (XRII) system. Maidment and Yaffe[17] demonstrated the applicability of such analysis by measuring the DQE of a scanned-slot mammographic imager, and Bissonette et al.[6] applied a cascaded systems model in describing the DQE of
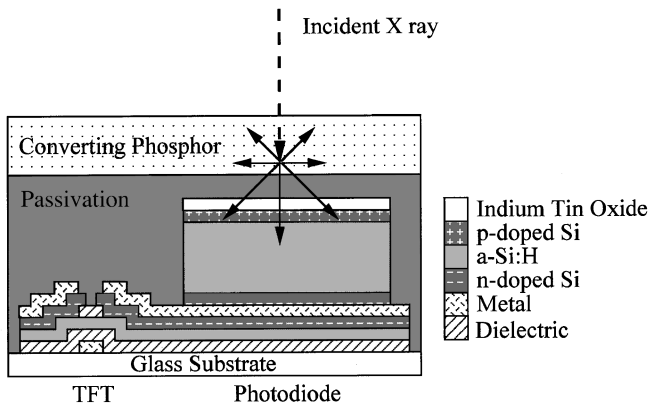
FIG. 2. Schematic cross section (not to scale) of a single *a*-Si:H imaging pixel.

FIG. 3. A quantum accounting diagram showing the various stages governing the signal and noise transfer for the *a*-Si:H imaging system. The three plots correspond to various spatial frequencies: solid line ($u=v=0$ mm^{-1}); dashed line ($u=v=5$ mm^{-1}); dotted line ($u=v=10$ mm^{-1}). For the lower spatial frequencies, absorption of primary x rays (stage 1) represents the quantum sink for the system. At the highest spatial frequency, however, a secondary quantum sink occurs at stage 3, indicating that the imaging performance is limited by the spatial resolution of the converter. See the text for details regarding each stage.

a video-based portal imaging system. The signal, noise, and DQE for flat-panel, *a*-Si:H x-ray imagers may be similarly analyzed.[18]

III. METHODS AND MATERIALS

A. A cascaded systems model for a flat-panel, x-ray imaging system

A schematic cross section of a single pixel from an *a*-Si:H AMFPI is shown in Fig. 2. A fraction of the x rays incident on the detector interact in the converting material to produce optical photons. These photons spread and are partially attenuated within the converter, and those that exit the lower surface of the screen may contribute to the measured signal. Photons transmitted through layers overlying the photodiode may interact in the intrinsic layer of the *a*-Si:H sensor, creating electron–hole ($e-h$) pairs which are collected by means of an applied electric field. The imaging signal is read out by switching the TFT to a conducting state via the voltage applied on the gate line, and the signal is passed along a data line and integrated by charge-sensitive amplifiers external to the array. The analog signals are then multiplexed, digitized, and sent to a computer.

This system and the physical processes which govern its performance can be represented schematically in a QAD as shown in Fig. 3. The stages shown in Fig. 3 are explained below, and only a cursory description of each is offered here: Stage 0 represents the Poisson-distributed incident x-ray distribution (normalized to unity); stage 1 represents absorption of incident x rays in the converting medium; stage 2 represents the generation and emission of optical photons in the converter; stage 3 represents the spread of these optical photons within the converter; stage 4 represents the coupling of optical photons to the active photodiode; and stage 5 represents the integration of quanta by the photodiode sensor. Sources of additive electronic noise are included at stage 5. Each stage is either a gain or a spatial spreading stage, and the various curves correspond to different values of spatial frequency. Note that for the zero-frequency ($u=v=0$) plot, the number of useful image quanta is unaffected by the spa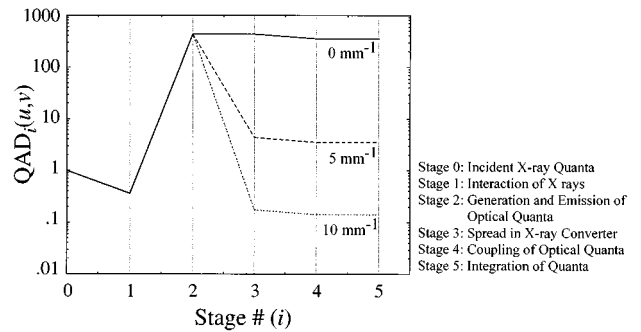tial spreading stages, since the MTF is unity. At higher frequencies, however, stochastic spreading results in a loss (blurring) of image information and a corresponding decrease in DQE. In the following subsections, the parameters governing the signal and noise transfer characteristics of the system are discussed for each stage in the QAD.

0. Stage 0: Incident x-ray quanta

A spectrum of Poisson-distributed incident x-ray quanta is considered [$S_0(u,v)=\bar{q}_0$].[10] For a given x-ray spectrum incident upon the imager, the mean fluence, $\bar{q}_0$, per unit exposure, X (in units of mR), is calculated as in Ref. 19:

$$\frac{\bar{q}_0}{X} = \int_0^\infty \frac{k q_{\mathrm{rel}}(E)}{E[\mu_{\mathrm{ab}}(E)/\rho]_{\mathrm{air}}} dE \quad (\text{units: x rays/mm}^2/\text{mR}).$$

(4)

The value of k is a constant (5.45×10^8 eV/g/mR) determined by the definition of the Roentgen and desired units, and $q_{\mathrm{rel}}(E)$ is the normalized incident x-ray spectrum. E has units of electron-volts (eV), and $[\mu_{\mathrm{ab}}(E)/\rho]_{\mathrm{air}}$ is the energy absorption coefficient (cm^2/g) for air.

1. Stage 1: Interaction of incident x-ray quanta in converter

Stage 1 is a gain stage representing the interaction of incident x-ray quanta in the converting medium, where $\bar{g}_1$ is the mean fraction of x rays that interact in such a way as to produce light. For an x-ray spectrum incident upon a converting material with interaction coefficient $[\mu(E)/\rho]$ and surface density δ (g/cm^2), the mean gain is given by

$$\bar{g}_1 = \frac{\int_0^{E_{\max}} q_0(E)(1-e^{-[\mu(E)/\rho]\delta})dE}{\int_0^{E_{\max}} q_0(E)dE}.$$

(5)

Since this interaction process obeys binomial statistics (i.e., either an x ray interacts to produce optical photons, or it does not), the associated gain-variance is given by Eq. (3b). For

an imaging system which relies upon indirect detection of x rays, $\bar{g}_1$ (the quantum efficiency of the converter) is the upper limit of the DQE.

2. Stage 2: Generation and emission of optical quanta

Stage 2 represents the combined effects of generation and emission of optical quanta from the x-ray converter. These two processes are discussed separately in Secs. III A 2 a and III A 2 b, but they are combined in a single stage in the QAD, since the effective gain and gain-variance of the combined processes are measurable quantities.[20–24] The quantum gain, $\bar{g}_2$, equals the product of the gains of the substages ($\bar{g}_2 = \bar{g}_{2a}\bar{g}_{2b}$), and the gain-variance involves the combined effects of conversion noise (substage 2a) and escape efficiency (substage 2b). The overall gain and gain-variance may be obtained from measured absorbed energy distributions (AEDs)[20–22,24] for a given converter, thereby ensuring that effects due to both the amount of energy absorbed and the amount of light exiting the converter are taken into account.[25]

a. Generation of optical quanta. For an incident x-ray spectrum, the average number of optical quanta produced per interacting x ray is given by

$$\bar{g}_{2a} = \frac{\int_0^{E_{max}} q_1(E)\bar{g}_{2a}(E)dE}{\int_0^{E_{max}} q_1(E)dE}, \tag{6}$$

where $q_1(E)$ is the spectrum of interacting x rays and $\bar{g}_{2a}(E)$ is the mean number of quanta generated per interacting x ray of energy E. The amount of energy deposited in the converter per interacting x ray is subject to fluctuation (conversion noise) and may be analyzed from AEDs.[13,20–22,24] For the case of monoenergetic x rays, the moments of the AED are related to the mean gain and gain-variance of the converter. In the case of an energy spectrum, the effective gain-variance is determined by averaging the moments of the monoenergetic AEDs over the absorbed spectrum and then combining the averaged moments to obtain the Swank factor or Poisson excess. As noted by Swank,[13] it is incorrect to average the Swank factor or Poisson excess over the spectrum directly.

b. Emission of optical quanta. Due to attenuation of optical photons within the converting medium, only a fraction, $\bar{g}_{2b}$, of the photons generated in the converter will exit toward the imaging array. Various models have been proposed to describe this process and estimate the escape fraction.[23] Since this process involves attenuation of quanta, it is assumed to follow binomial statistics, with gain-variance given by Eq. (3b).

3. Stage 3: Spatial spreading of optical quanta in converting screen

Stage 3 describes the stochastic spreading of optical photons in the converting medium, characterized by the screen MTF, $T_3(u,v)$. This is the first stage for which frequency dependence becomes evident, and it is seen in Fig. 3 that blurring in the screen reduces the QAD at nonzero spatial frequencies. In the general case of an x-ray spectrum incident upon the converter, an empirical screen MTF obtained with the appropriate incident spectrum may be used. Although the physical processes of spatial spreading (stage 3) and self-attenuation (stage 2b) of optical quanta in the converter are coincident, the order of these stages in the QAD is unimportant, since stochastic spreading and binomial selection stages commute.

4. Stage 4: Coupling of optical quanta

Stage 4 is a series of binomial selection substages representing the coupling of optical quanta to the detector elements. The substages described below represent four processes which affect the coupling efficiency: (a) transmission of photons through layers overlying the photodiode, (b) reflection at interfaces between overlying layers, (c) absorption of photons in the photodiode and conversion to $e-h$ pairs, and (d) collection of charge from the photodiode. Since each substage follows binomial statistics the coupling efficiency, $\bar{g}_4$, is given by Eq. (3a) and the gain-variance by Eq. (3b). Furthermore, the order in which each substage is considered is unimportant, since binomial selection stages commute. The coupling efficiency of the photodiodes can be measured, as shown in Fig. 2 of the companion paper.[5]

a. Transmission through layers overlying photodiode. As shown schematically in Fig. 2, a number of layers overlay the i-layer of the photodiode and partially attenuate optical photons emitted from the converter. These layers include: a thin passivation layer which protects the surface of the array; a semitransparent, conductive layer of indium tin oxide which provides an equipotential surface for the applied photodiode bias voltage; and a layer of doped material which provides a semiconductor junction. The mean fraction of optical photons transmitted through each layer can be computed from the optical spectrum, $q_{i-1}(\lambda)$, the linear attenuation coefficient, $\mu(\lambda)$, and thickness, d, of each layer,

$$\bar{g}_i = \frac{\int_{\lambda_{min}}^{\lambda_{max}} q_{i-1}(\lambda)e^{-\mu(\lambda)d}d\lambda}{\int_{\lambda_{min}}^{\lambda_{max}} q_{i-1}(\lambda)d\lambda}, \tag{7}$$

where λ represents the wavelength of the optical quanta, and λ_{min} and λ_{max} are the shortest and longest wavelengths, respectively, in the optical spectrum. Transmission of quanta through each layer obeys binomial statistics, and the effective gain for substage 4a is given by a linear combination of the individual gains computed using Eq. (7) for each layer.

b. Reflection at layer interfaces. Substage 4a describes the transmission of optical quanta through layers overlying the photodiode, but at each layer interface optical quanta may be reflected due to unmatched indexes of refraction between materials in adjacent layers. Such reflections tend to reduce the total coupling efficiency of the detector.[16] Since this process obeys binomial statistics (either a photon is reflected or it is transmitted), the net effect of reflections at all interfaces can be described by a single substage, 4b. Further-

more, the gain and gain-variance corresponding to each interface can be combined [Eqs. (3a) and (3b)] to describe the transfer across all of the interfaces.

c. Absorption of optical photons and conversion to $e-h$ pairs. Substage 4c describes the absorption of optical photons and conversion to $e-h$ pairs in the i-layer of the a-Si:H photodiode. Although the processes of absorption and conversion could be treated in separate substages, for succinctness they are combined. For a sufficiently thick ($\geqslant 1\mu$m) i-layer, it is expected that nearly all of the incident optical photons will be absorbed.[26] Similarly, it is assumed that each absorbed photon results in the creation of a single $e-h$ pair. Therefore, this stage is characterized by a gain and gain-variance of $\bar{g}_{4c}\sim 1$ and $\sigma^2_{g_d}\sim 0$, respectively (i.e., this stage approximates a deterministic, unity gain process).

d. Collection of $e-h$ pairs. Due to metastable trapping states in the intrinsic a-Si:H,[27] only a fraction of the charge generated in the photodiode on a given frame is collected as signal. The fraction of charge lost to traps depends on the electric field across the photodiode, which in turn is determined by a number of operating parameters, such as photodiode bias voltage and signal level.[28] The mean number of electrons collected per absorbed optical photon is the mean gain for this substage and, assuming that the electrical quanta either fall into a trapping state or do not, the substage is taken to obey binomial statistics, with gain-variance given by Eq. (3b). In radiography, where an image is acquired following a brief exposure, the average gain is directly related to the quantity Q_{trap} described in the companion paper.[5] Although the charge lost to traps could be at least partially collected by readout of subsequent frames, it is assumed in this discussion that only a single frame is read following the radiographic exposure.

In fluoroscopy, where frames are continually read under irradiation, the situation is somewhat different. The states responsible for charge trapping are metastable, and trapped charge is released over a characteristic lifetime.[27] Therefore, charge generated and trapped in previous frames may be released and collected in the current frame. Under conditions of constant irradiation, signal equilibrium is reached when the amount of charge entering traps equals the amount being released, and the effective mean gain approaches unity. The effect of charge trapping and release upon signal size is discussed in the companion paper (Fig. 9),[5] where radiographic and fluoroscopic signal response are compared. The phenomena of charge trapping and release have an interesting effect on the noise measured in fluoroscopic mode and are described in Sec. III B 3.

5. Stage 5: Integration of quanta by photodiode

Stage 5 is a deterministic spreading stage representing the integration of quanta by the photodiode and characterized by the presampling pixel MTF, $T_5(u,v)$. Since both the frequency-dependent signal (squared) and NPS are operated upon identically in a deterministic spreading stage, there is no net effect upon DQE. For this reason, the QAD shows no

degradation at stage 5, but the stage is included explicitly so that its effect upon the signal and noise, individually, is taken into account.

Discrete photodiode a-Si:H arrays show excellent isolation of signal between neighboring pixels, with MTF determined accurately by the sampling aperture.[29,30] For such imagers, however, only a fraction of the total pixel area is sensitive to light, and the sampling aperture, a_{pd}, is related to the pixel pitch, a_{pix}, by the fill factor, f_{pd},

$$a^2_{\text{pd}}=f_{\text{pd}}a^2_{\text{pix}}. \tag{8}$$

Reflection of optical photons from metal lines, which could affect the sensitivity and MTF of the pixel, is found empirically to be small and is assumed negligible.

For analysis of the presampling signal and noise properties of individual photodiode sensors, the nominal unit area is given by that of the optically sensitive photodiode; therefore, only the size of the sampling aperture, a_{pd}, is relevant. Analysis of the sampled properties of the imagers,[31] however, would involve the sampling interval, a_{pix}, and fill factor explicitly. This paper describes empirical and theoretical aspects of the presampling signal and noise transfer, and analysis of the sampled signal and noise, including the effects of aliasing, is beyond the scope of this paper.

6. Additive electronic noise

Four sources of additive electronic noise are considered: (a) intrinsic noise from the a-Si:H pixel, σ_{pix}; (b) noise due to voltage fluctuations on the gate and bias lines, σ_{lin}; (c) noise from the amplifier, σ_{amp}; and (d) digitization noise from the analog-to-digital converters (ADCs), σ_{ADC}. All signal and noise values will be referred to the amplifier input in units of electrons, and the amplifier gain does not appear explicitly in the analysis. Since each noise source is statistically independent, the variances add, giving a total additive variance, σ^2_{add},

$$\sigma^2_{\text{add}}=\sigma^2_{\text{pix}}+\sigma^2_{\text{lin}}+\sigma^2_{\text{amp}}+\sigma^2_{\text{ADC}}. \tag{9a}$$

The additive noise components in Eq. (9a) are discussed briefly below.

a. Additive intrinsic pixel noise. The intrinsic pixel noise may be analyzed by considering individual noise components, including photodiode and TFT $1/f$ noise and shot noise and TFT thermal noise.[32] Calculations which use the measured noise power spectra of photodiodes[33] and TFTs[34] indicate that TFT thermal noise is typically the dominant component under relevant array operating conditions. Considering the pixel circuit as a capacitor (the photodiode) in series with a resistor (the TFT), the pixel noise due to TFT thermal noise is given by[35]

$$\sigma^2_{\text{pix}}=k_B T C_{\text{pd}}\left[1-\exp\left(\frac{-2\tau}{R_{\text{on}}C_{\text{pd}}}\right)\right]. \tag{9b}$$

In Eq. (9b), k_B is Boltzmann's constant, T is the absolute temperature, C_{pd} is the capacitance of the photodiode (typically ~ 1 pF, depending on pixel design), τ is the sampling time (typically ~ 500 μs), and R_{on} is the resistance of the

TFT in the conducting state (~ 1 MΩ).[36] For $\tau \gg R_{\text{on}} C_{\text{pd}}$, the term in parentheses approaches unity. Furthermore, this noise component is manifest twice—once as a result of the thermal noise integrated by the amplifier on the current cycle, and once as a result of the thermal noise integrated by the photodiode on the previous cycle. Since these contributions are equal and independent, the resulting variance is doubled,

$$\sigma_{\text{pix}}^2 \approx 2 k_B T C_{\text{pd}}. \tag{9c}$$

This analysis is consistent with results presented by Schiebel *et al.*[1]

b. Additive capacitive coupling noise. A second source of additive noise is due to fluctuations in voltage on the gate and bias lines. Overlap capacitance within the TFTs and capacitance between gate, bias, and data lines couple these fluctuations to the data lines, resulting in noise, σ_{lin}, at the preamplifier input. The magnitude of the coupled noise has been estimated from measurements,[37] and it can be minimized through careful array design and/or correlated double sampling.

c. Additive amplifier noise. An approximation of the noise due to the integrating amplifier may be obtained using a model which considers a capacitance, C_{in}, connected to its input. As detailed by Motchenbacher,[38] the amplifier may be modeled as a noiseless device with a spectral voltage noise source in series with the inputs. The variance in charge due to the amplifier is obtained by integrating over all frequencies the voltage noise (squared) multiplied by C_{in}^2. The result is that the amplifier noise is given by a constant ''base'' noise plus a term which increases with C_{in}. For large area AMFPIs, this is an important consideration, since C_{in} can be large (~ 50–100 pF) due to the capacitance of the data lines.

d. Additive digitization noise. Finally, digitization noise due to ADCs can be included in the total additive noise. This noise source is due to the quantization of the signal amplitude and has been discussed in detail elsewhere.[39–41]

B. Signal and noise transfer

In this section, expressions are derived for the x-ray sensitivity and noise for individual pixels of an *a*-Si:H imager. The x-ray sensitivity (Sec. III B 1) describes the average signal collected from a pixel per unit exposure and is proportional to the product of the quantum gains described in Sec. III A. The individual pixel noise under x-ray irradiation (Sec. III B 2) is obtained by calculating the presampling NPS and integrating over all spatial frequencies. In Sec. III B 3, the effect of charge trapping and release on the noise is discussed, and in Sec. III B 4 the effect of nonlinearity and saturation on the noise is considered.

1. Signal transfer and x-ray sensitivity

The cascaded systems approach provides a straightforward means of calculating the average signal collected under x-ray irradiation using Eq. (1a). The mean signal response of the system is related simply to a linear combination of the system gains. Defined as the average signal collected per unit exposure, the x-ray sensitivity is the average slope of the signal response, given by

$$\Gamma = a_{\text{pd}}^2 \frac{\overline{q}_0}{X} \, \overline{g}_1 \overline{g}_2 \overline{g}_4 \quad \text{(units: } e/\text{mR)}. \tag{10}$$

This analysis describes the average signal read for a given uniform exposure, assuming a linear detector response. Such an assumption is valid across a large fraction (up to $\sim 90\%$) of the sensitive range of *a*-Si:H imaging pixels at normal operating photodiode bias voltage.[5,42]

2. Noise power spectrum and individual pixel noise

Considering the QAD of Fig. 3, the presampling NPS, $S_5(u,v)$, can be determined from Eqs. (2a), (2b), (2c) and the properties discussed in Sec. III A. As derived in Appendix A, Eq. (A5), the presampling NPS is

$$S_5(u,v) = a_{\text{pd}}^4 \overline{q}_0 \overline{g}_1 \overline{g}_2 \overline{g}_4 [1 + \overline{g}_4 (\overline{g}_2 + \epsilon_{g_2}) T_3^2(u,v)]$$
$$\times T_5^2(u,v) + S_{\text{add}}(u,v), \tag{11}$$

where $S_{\text{add}}(u,v)$ is the NPS associated with the additive noise sources described in Sec. III A 6.

The variance is given by the two-dimensional integral over the NPS.[10] Assuming that the system is ergodic, this variance describes the fluctuations in signal from either a collection of pixels in a single frame or from repeated measurements of a single pixel. As shown in Appendix B, Eq. (B4), the individual pixel variance at stage 5 of the imaging chain is

$$\sigma_{N_5}^2 = a_{\text{pd}}^2 \overline{q}_0 \overline{g}_1 \overline{g}_2 \overline{g}_4 [1 + \overline{g}_4 (\overline{g}_2 + \epsilon_{g_2}) s] + \sigma_{\text{add}}^2, \tag{12}$$

where the ''sharpness factor,'' s, is defined as in Eq. (B3) in relation to the system MTFs and accounts for the effects of image blur on the noise,

$$s \equiv a_{\text{pd}}^2 \int_{-\infty}^{+\infty} \int_{-\infty}^{+\infty} T_3^2(u,v) T_5^2(u,v) \, du \, dv. \tag{13}$$

Note that the sharpness factor has values $0 \leqslant s \leqslant 1$, where s is unity for the case of an ideal converter [i.e., for $T_3(u,v) = 1$]. The result for the individual pixel variance shown in Eq. (12) accounts for the magnitude of the incident fluence, the quantum gains and gain-variances of the imaging system, and image blur described by the system MTFs (contained in the sharpness factor).

For comparison, a simple derivation of the ''zero-frequency'' pixel variance may be obtained by considering counting statistics alone. Analogous to Eq. (2a) is the relation for zero-frequency noise transfer,[8]

$$\sigma_{N_i}^2 = \overline{g}_i^2 \sigma_{N_{i-1}}^2 + \sigma_{g_i}^2 \overline{N}_{i-1} + \sigma_{\text{add}_i}^2. \tag{14a}$$

Considering only the gain stages of the QAD and taking $\sigma_{N_0}^2 = \overline{N}_0 = a_{\text{pd}}^2 \overline{q}_0$ yields the following zero-frequency result:

$$\sigma_{N_5}^2 = a_{\text{pd}}^2 \overline{q}_0 \overline{g}_1 \overline{g}_2 \overline{g}_4 [1 + \overline{g}_4 (\overline{g}_2 + \epsilon_{g_2})] + \sigma_{\text{add}}^2, \tag{14b}$$
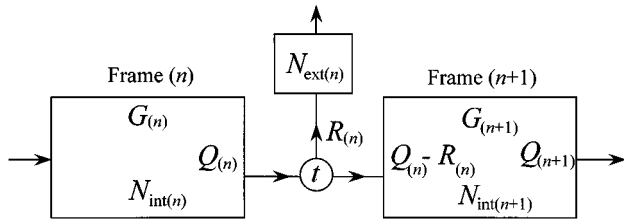
FIG. 4. Schematic diagram illustrating the process of charge trapping and release, which results in charge carryover, or image lag, between successive frames.

which differs from Eq. (12) by the sharpness factor. The two relations are equal in the case $s=1$; therefore, the zero-frequency case is identical to assuming either a perfect converting screen or an infinitely large photodiode. Compared to the frequency-dependent analysis, the zero-frequency approach always overestimates the individual pixel variance, and consideration of the frequency-dependent noise transfer properties as derived in Appendices A and B is necessary in order to account for the effect of image blur.

3. The effect of charge trapping and release (image lag) on noise

For an imager operated in fluoroscopic mode, analysis of the noise transfer properties should account for the effects of charge trapping and release (which cause charge carryover between frames, visually perceived as ''lag'') described in Sec. III A (substage 4d). Charge carryover reduces the fluctuations in signal read from a pixel by correlating information between frames. This effect has been noted by others,[43,44] and the simple deterministic approximation considered here is similar to that of Matsunaga *et al.*[44] Figure 4 summarizes the model describing the effect of charge carryover on pixel noise. For the nth frame, $G_{(n)}$ is the number of photogenerated electrons, $Q_{(n)}$ is the number of electrons available for readout, and $R_{(n)}$ is the amount of charge read out. $N_{\text{int}(n)}$ and $N_{\text{ext}(n)}$ are the number of additive noise electrons generated within and external to the photodiode, respectively, in frame (n). The parameter t is defined as the fraction of $Q_{(n)}$ which is trapped in the photodiode after readout (equal to the quantity Q_{trap} in the companion paper[5]).

The individual pixel noise is related to the variance in $R_{(n)}$, $\sigma^2_{R_{(n)}}$, and is dependent upon the parameter t. As shown in Appendix C, the variance in pixel signal under fluoroscopic operation is

$$\sigma^2_{R_{(n)}} = \left(\frac{1-t}{1+t}\right)(\sigma^2_{G_{(n)}} + \sigma^2_{N_{\text{int}(n)}}) + \sigma^2_{N_{\text{ext}(n)}}. \tag{15}$$

The term $\sigma^2_{G_{(n)}}$ corresponds to fluctuations due to incident x-ray quanta, whereas $\sigma^2_{N_{\text{int}(n)}}$ and $\sigma^2_{N_{\text{ext}(n)}}$ correspond to the additive noise. For the case of zero charge carryover ($t=0$), Eq. (15) reduces to Eq. (12). In general, $0<t<1$, and charge carryover suppresses fluctuations in the number of electrons collected from the photodiode. Since all of the significant

additive noise sources discussed in Sec. III A occur external to the photodiode, $\sigma^2_{N_{\text{int}(n)}} \approx 0$ and $\sigma^2_{N_{\text{ext}(n)}} \approx \sigma^2_{\text{add}}$, and combining Eqs. (12) and (15) gives

$$\sigma^2_{N_5} = \left(\frac{1-t}{1+t}\right) a^2_{\text{pd}} \bar{q}_0 \bar{g}_1 \bar{g}_2 \bar{g}_4 [1 + \bar{g}_4(\bar{g}_2 + \epsilon_{g_2})s] + \sigma^2_{\text{add}}. \tag{16}$$

4. The effect of signal nonlinearity and saturation on noise

Despite the highly linear response exhibited by a-Si:H imaging pixels, at sufficiently high signal levels the linearity degrades and the pixels saturate. The above formulas for signal and noise assume a linear detector response, but as the linearity degrades, the output noise (and sensitivity) is suppressed since the effective gain of the system is reduced. At saturation the quantum noise is completely suppressed,[10] and the output noise is due solely to additive noise sources. These effects may be incorporated in the noise analysis by considering a signal response function, $\bar{N}_5(X)$, plotted versus exposure (as in Fig. 9 of the companion paper[5]) or versus the average number of incident x rays, $\bar{N}_0$. The slope of this function defines the dynamic, exposure-dependent gain of the system:

$$\gamma \equiv \frac{d}{d\bar{N}_0} \bar{N}_5(X). \tag{17}$$

At low signal levels where detector response is linear, γ is given by the product of the system gains ($\gamma = \bar{g}_1 \bar{g}_2 \bar{g}_4 \propto \Gamma$). At higher signal levels, however, γ decreases rapidly and approaches zero at saturation.

With this definition and Eq. (16), the dynamic gain may be included in the noise analysis by substituting $\gamma = \bar{g}_1 \bar{g}_2 \bar{g}_4$, where the dependence upon exposure arises from decreased signal collection efficiency (included in $\bar{g}_4$) at high signal levels. Thus, the pixel variance can be written as

$$\sigma^2_{N_5} = \left(\frac{1-t}{1+t}\right) a^2_{\text{pd}} \bar{q}_0 \gamma \left[1 + \frac{\gamma}{\bar{g}_1 \bar{g}_2}\left(\frac{\gamma}{\bar{g}_1 \bar{g}_4} + \epsilon_{g_2}\right)s\right] + \sigma^2_{\text{add}}. \tag{18}$$

In this analysis, accurate knowledge of all system parameters is still necessary, and incorporation of the dynamic gain in no way represents a normalization of the calculations to measurements. Inclusion of the dynamic gain simply accounts for reduced efficiency at high signal levels. For low signal levels, Eq. (18) reduces to Eq. (16). For signal levels above saturation ($\gamma \to 0$), the noise at the output of the detector is given solely by the additive noise sources, as expected.

C. Empirical determination of signal and noise properties

In order to provide partial verification of the theoretical analysis described in Sec. III B, theoretical predictions of signal and noise for individual pixels were compared against empirically determined values. These empirical data were acquired radiographically and fluoroscopically from an imager incorporating a 1536×1920 pixel array with a pixel

pitch of 127 μm, the construction and operation of which are described in the companion paper.[5] Measurements were performed using three commercially available Gd$_2$O$_2$S:Tb converters: Lanex Fine ($\sim$34 mg/cm^2), Lanex Regular ($\sim$70 mg/cm^2), and Lanex Fast-B ($\sim$133 mg/cm^2) and using an x-ray source also described in Ref. 5. The exposure or exposure rate at the surface of the imager was measured using an ion chamber and dosimeter (Keithley models 96035 and 35050A, respectively). Specifically, the calculated x-ray sensitivity of individual pixels was compared against the measurements reported in Refs. 5 and 45.

The noise properties of individual pixels were measured under x-ray irradiation as a function of exposure to the detector. At a given exposure, N samples from each pixel were acquired to form a realization, and each realization was divided into n groups. For a given realization, the standard deviation in pixel signal, σ_n, was computed for each group, and the results from the n groups were averaged to yield the noise value. Since several minutes were typically required to obtain a single realization, it was necessary to account for correlated fluctuations arising from drift in output of the x-ray tube. To eliminate this noise component, the analysis method described above was performed using realizations consisting of the difference in signal from pairs of widely separated pixels (with the resulting noise value divided by $\sqrt{2}$ to account for the subtraction).[46] The resulting noise value, $\bar{\sigma}$, was reported at the mean exposure for each pixel pair, and the associated error in $\bar{\sigma}$ was found by computing the standard deviation in σ_n over the n groups and dividing by $\sqrt{n}$.[46]

Measurements of the individual pixel noise were performed at 90 kVp over the entire signal range of the detector. All noise measurements were performed at SID=61 cm, and the exposure to the detector was controlled by adjusting the tube current at constant frame time ($\sim$1 s for measurements performed in fluoroscopic mode). All other array operational parameters were the same as for the x-ray sensitivity measurements.[5] Realizations consisting of 200 samples each were obtained for eight pixels (4 pixel pairs), and each realization was divided into 10 groups. (Hence, $N=200$ and $n=10$.) Each pixel pair consisted of two pixels lying along the same gate line; therefore the above analysis eliminates correlated noise arising from drift in x-ray tube output as well as that due to fluctuations in gate and photodiode bias line voltage (σ_{lin}). The resulting noise value is due almost entirely to fluctuations in the input quanta, inherent pixel noise, and additive amplifier noise.

D. Comparison of empirical and theoretical signal and noise

Empirical x-ray sensitivity and individual pixel noise were compared to theoretical results obtained using Eqs. (10) and (18), respectively. This section describes the manner in which the parameters appearing in Eqs. (10) and (18) were estimated. The incident x-ray spectra were approximated using Ref. 47. The quantum efficiency of the Gd$_2$O$_2$S:Tb converters was obtained using Eq. (5), with the interaction
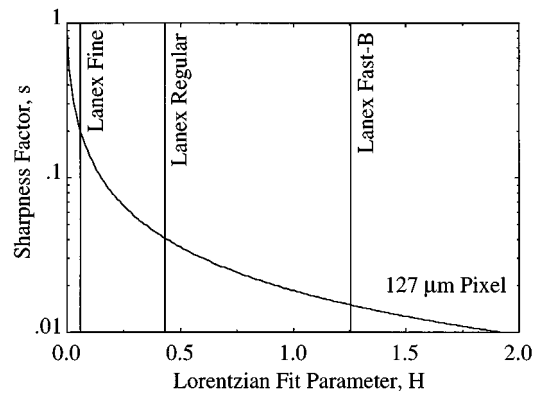

FIG. 5. The sharpness factor, s, computed as a function of the Lorentzian MTF fit parameter (blur), H, for a 127 μm pitch array. The values of H for three Lanex screens are indicated.

coefficients[48] of the component materials combined relative to weight. Direct detection of x rays by the thin ($\sim$1 μm) a-Si:H photodiode is small ($\sim$0.01%) and, although each direct interaction can produce thousands of secondary electrons,[49] this effect was neglected in the present analysis. The energy-dependent quantum gain and Poisson excess of the converters was obtained from measured AEDs,[20] which describe the combined processes of generation and emission of optical quanta, as described in Sec. III A (stage 2). The MTF of Lanex Fine, Regular, and Fast-B converters was approximated by a Lorentzian fit to empirical data (provided by P. C. Bunch, Ph.D., Eastman Kodak Co.):

$$T_3(u,v) \approx \frac{1}{1 + H \cdot (u^2 + v^2)}, \tag{19}$$

where H is a fitting parameter describing the relative blur of the screen.

The coupling efficiency of the photodiode was estimated by integrating the measured pixel quantum efficiency[5] over the incident emission spectrum.[50] This estimate suggests that absorption in the overlying p-layer and collection of charge from the intrinsic layer dominate the total coupling efficiency, and absorption in other overlying layers and reflection at interfaces is small in comparison. The charge carryover parameter, t, was measured as a function of photodiode bias voltage and signal level as described in the companion paper[5] and taken as empirical input to the theoretical model. The dynamic response, γ, was obtained by calculating the slope of the empirical signal response[5] for a given set of operating conditions.

The pixel MTF was estimated as in Eq. (B1). Although this neglects the irregular shape of the photodiode, it gives reasonable agreement with empirical results.[29,30] The sharpness factor, s, was calculated using Eq. (13). Figure 5 shows the sharpness factor for a 127 μm pitch pixel as a function of the Lorentzian (blur) parameter, H. Since the sharpness factor is a rapidly decreasing function of H, it has a significant effect on the individual pixel noise even for a system incorporating a converting screen with relatively high MTF.

TABLE I. Summary of conditions and imager configurations for DQE calculations.

	Radiography	Fluoroscopy	Mammography
Energy (kVp)	110	80	30
Anode	Tungsten	Tungsten	Molybdenum
Filtration	2.75 mm Al	2.75 mm Al	0.03 mm Mo
Exposure range (mR)	0.03–3	0.0001–0.01	0.6–240
Mean exposure (mR)	0.2	0.002	5
Pixel pitch (μm)	100	200	50
X-ray Converter	70 mg/cm^2 Gd$_2$O$_2$S:Tb	70 mg/cm^2 Gd$_2$O$_2$S:Tb	34 mg/cm^2 Gd$_2$O$_2$S:Tb
	150 mg/cm^2 CsI:Tl	150 mg/cm^2 CsI:Tl	100 mg/cm^2 CsI:Tl
	250 mg/cm^2 CsI:Tl	250 mg/cm^2 CsI:Tl	

The additive noise sources were assumed to be independent of signal size and described by Eq. (9a). The total additive noise was determined from measurements performed in the absence of x rays, with the intrinsic pixel noise calculated using Eq. (9c).

E. The detective quantum efficiency for a flat-panel, x-ray imaging system

The DQE is an accepted means of characterizing the observer-independent performance of imaging systems[51] and describes the transfer of the signal-to-noise ratio, SNR, through the imaging chain. Maximization of the DQE can be adopted as a criterion for system optimization, and the model described above is a useful tool for examining the effect of varying system parameters on the DQE.

The cascaded systems model can be used to calculate the frequency-dependent signal, noise, and DQE, but many of the important signal and noise transfer properties (as well as the maximum achievable performance of the imager) are described by the zero-frequency detective quantum efficiency, DQE(0). Such zero-frequency analysis is analogous to integrating the incident quanta, $q_{i-1}(x,y)$, over all space and applying the input at a single point at stage i (i.e., it ignores all blurring processes). To examine the effect of fill factor upon DQE(0), the geometric pixel area, a_{pix}^2, is considered, with the fill factor then included as a term in the coupling efficiency. Accounting for fill factor in this manner is valid at zero spatial frequency, since loss of quanta due to photosensitive regions of the pixel is equivalent (at zero frequency) to a simple binomial selection. This process is included as an additional substage in stage 4 (coupling efficiency), with average gain given by the fill factor. The DQE(0) for the entire pixel is then obtained by calculating the square of the SNR at stage 5 (the presampling stage) in proportion to that at stage 0 and evaluating the ratio at zero-frequency, yielding

$$\text{DQE}(0) = \frac{\bar{g}_1 \bar{g}_2 \bar{g}_4}{1 + \bar{g}_4 (\bar{g}_2 + \epsilon_{g_2}) + \dfrac{\sigma_{\text{add}}^2}{a_{\text{pix}}^2 \bar{q}_0 \bar{g}_1 \bar{g}_2 \bar{g}_4}}, \qquad (20)$$

where $\bar{g}_4$ now includes the fill factor. For simplicity, the effects of charge carryover and nonlinearity are assumed negligible. These could be included as described in Secs. III B 3 and III B 4, respectively, but these effects tend to obscure the more fundamental properties governing the DQE. Analysis of the spatial frequency-dependent DQE of the imager is beyond the scope of this paper and is the subject of future investigation.

Potential performance of a-Si:H imagers is explored by evaluating the DQE(0) under a variety of clinical applications, imager configurations, and readout modes. Three clinical applications are considered—radiography, fluoroscopy, and mammography. Similar to the requirements outlined by Zhao and Rowlands,[4] the nominal spectra,[47,52] exposure conditions,[53,54] and imager configurations relevant to each application are summarized in Table I. For each application, the pixel pitch of the a-Si:H array and choice of converter were selected to give spatial resolution generally consistent with clinical requirements. For each application, the effect of exposure level, amplifier noise, and fill factor on DQE(0) was investigated for two choices of x-ray converter material: Gd$_2$O$_2$S:Tb and CsI:Tl.

For both radiography and fluoroscopy, a Gd$_2$O$_2$S:Tb screen with a coverage of ~70 mg/cm^2 (Lanex Regular) was assumed, whereas for mammography the coverage was ~34 mg/cm^2. The relatively long afterglow characteristic of Gd$_2$O$_2$S:Tb converters possibly makes them inappropriate for clinical fluoroscopy, and calculation of DQE(0) under such conditions assumes a hypothetical converter with quantum efficiency, gain, and Poisson excess equivalent to that of Lanex Regular, neglecting afterglow. The quantum efficiency of the Gd$_2$O$_2$S:Tb screens was calculated for various incident spectra using Eq. (5), and the quantum gain and Poisson excess were computed from measured AEDs[20] as described in Sec. III A 2.

In addition, two thicknesses of CsI:Tl screen were chosen for radiography and fluoroscopy: (1) ~150 mg/cm^2, corresponding to the thickest input phosphor found in commercially available XRIIs,[55] and (2) ~250 mg/cm^2, reported by Wieczorek *et al.*[56] For mammography, a thinner (~100 mg/cm^2) screen was assumed. The quantum efficiency of the CsI:Tl converters is computed using Eq. (5), and the quantum gain and Poisson excess were calculated as described in Sec. III A 2 using published results.[13,22,23]

Finally, the performance of a 100 μm pitch fluoroscopic imager was analyzed for two readout modes: (1) "full-resolution" mode, in which the array is operated as described above, and (2) "half-resolution" mode, in which two rows of pixels are simultaneously addressed, reducing the

TABLE II. Imaging system parameters calculated at 90 kVp.

Parameter	Lanex Fine	Lanex Regular	Lanex Fast-B
$\bar{g}_1$	0.28	0.47	0.67
$\bar{g}_2$	600	1250	1420
ϵ_{g_2}	410	470	510
s	0.20	0.04	0.02
f_{pd}	0.35	0.35	0.35
$\bar{g}_4$	0.80	0.80	0.80

spatial resolution in one direction but doubling the maximum frame rate. These readout modes offer the potential of using the same 100 μm pitch array for both radiography (at full-resolution) and fluoroscopy (at half-resolution).[5]

IV. RESULTS

A. Imaging system parameters

The system parameters described in Sec. III A were calculated for a variety of incident x-ray spectra, and the results (at 90 kVp) are shown in Table II. The quantum efficiency ($\bar{g}_1$), quantum gain ($\bar{g}_2$), and Poisson excess (ϵ_{g_2}) for three Lanex screens used in the measurements are shown. For a given kVp, Lanex Fine has the lowest quantum efficiency, quantum gain, and Poisson excess, and Lanex Fast-B has the highest. For higher kVp, the quantum efficiency of each screen decreases, while the quantum gain and Poisson excess increase. Also shown are the sharpness factor for each screen in combination with the 127 μm pitch array, the fill factor (f_{pd}) for the array, and the coupling efficiency of the photo-diodes ($\bar{g}_4$).

B. X-ray sensitivity

Figure 6 shows the results of x-ray sensitivity measurements for the 127 μm pitch a-Si:H array in combination with
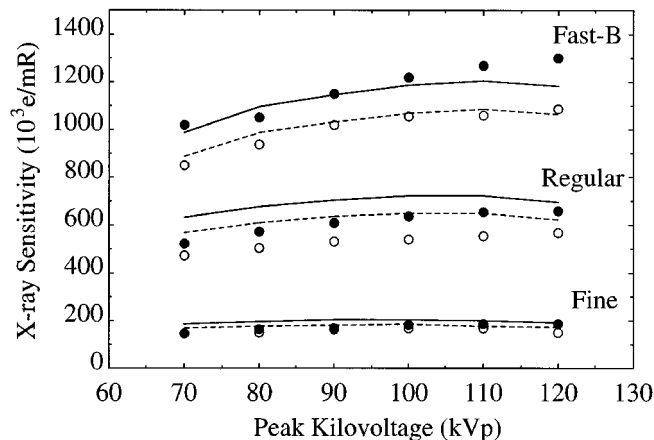
FIG. 6. Empirical and theoretical x-ray sensitivity vs peak tube potential (kVp) for the 127 μm pitch array in combination with three Lanex converters in fluoroscopic and radiographic modes. The open circles (○) and dashed lines correspond to measurements and calculations, respectively, for radiographic operation, whereas the closed circles (●) and solid lines correspond to fluoroscopic operation.

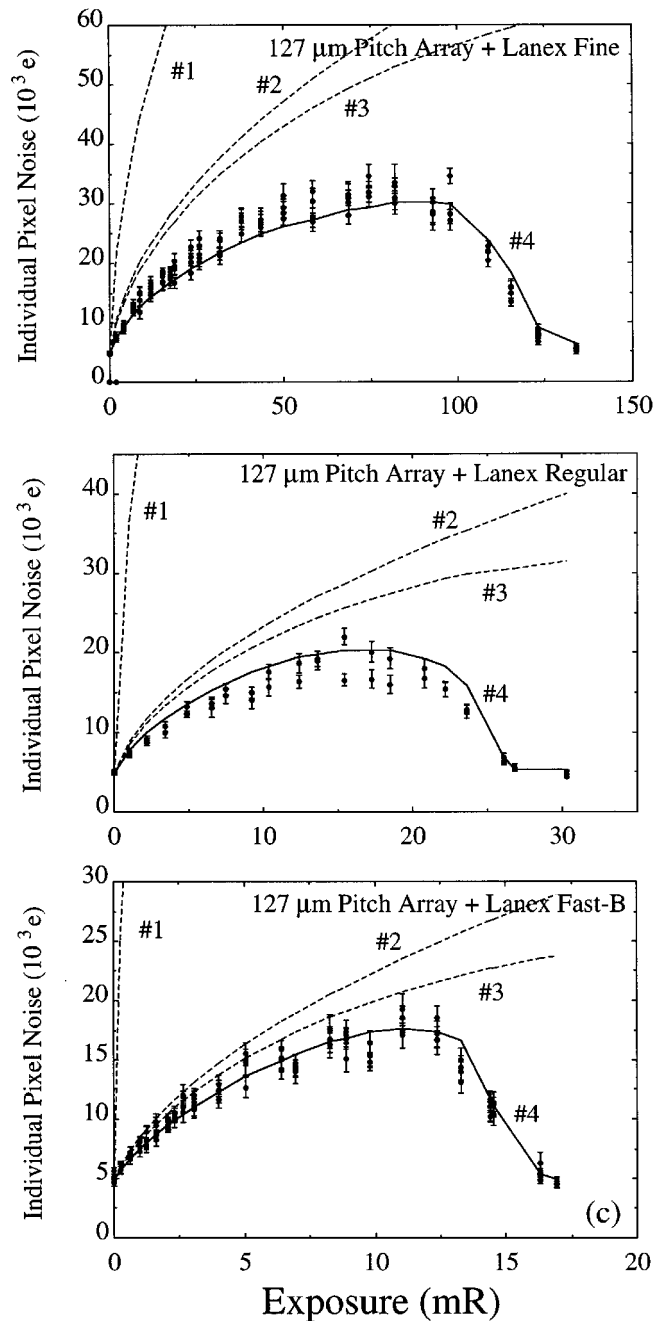FIG. 7. Empirical and theoretical individual pixel noise vs x-ray exposure for the 127 μm pitch array in combination with (a) Lanex Fine, (b) Lanex Regular, and (c) Lanex Fast-B in fluoroscopic mode. The four theoretical curves show the results of calculations which cumulatively include (1) zero-frequency counting statistics only [Eq. (14b)], (2) the effect of image blur [Eq. (12)], (3) the effect of image lag [Eq. (16)], and (4) (solid line) all of these effects and signal nonlinearity [Eq. (18)].

a variety of x-ray converters. The circles correspond to empirical measurements as reported in the companion paper,[5] and the lines represent theoretical results obtained using Eq. (10). Reasonable agreement between theory and measurement is observed for incident spectra ranging from 70 to 120 kVp. Measurements in fluoroscopic mode show slightly enhanced x-ray sensitivity consistent with the discussion of

Sec. III A 4 (substage 4d). Reasonable agreement was also observed for the x-ray sensitivity measured using a lower resolution array.[45]

C. Individual pixel noise under x-ray irradiation

The noise measured from individual pixels under x-ray irradiation is shown in Figs. 7(a), 7(b), and 7(c) for the 127 μm pitch array in combination with a Lanex Fine, Regular, and Fast-B screen, respectively. These measurements were performed at 90 kVp with the array operated in fluoroscopic mode. In each case, the noise (in units of electrons) is plotted versus exposure (mR), and the abscissae are very different for the three cases due to the differences in gain between the screens. Measurements reported at 0 mR were performed in the dark and correspond to the total additive noise ($\sim$5000 e) of the present imaging system. At relatively low exposures, the noise increases as the square root of the exposure. At higher signal levels, however, the noise increases less rapidly, and as the sensor approaches saturation the noise reduces to the additive noise level.

The individual pixel noise was calculated as a function of exposure for the three screens, and the results are superimposed in Fig. 7. The curves labeled #1–#4 incrementally demonstrate the effect of including image blur, lag, and nonlinearity in the pixel noise calculations. Curve #1, calculated using Eq. (14b), overestimates the actual noise because it ignores all of these effects. Curve #2, calculated using Eq. (12), accounts for the effect of image blur, and curve #3 accounts for the effect of charge carryover by Eq. (16). Finally, curve #4 (solid line) was calculated using Eq. (18) and accounts for all of the effects discussed in Sec. III B. When all effects are considered, excellent agreement between theory and measurement for three screens across the entire sensitive range of the pixel is observed.

The effect of charge carryover on the individual pixel noise was examined empirically by varying both the mode of array operation (radiographic or fluoroscopic) and the operating parameters known to affect charge trapping and release (such as photodiode bias voltage). At a given exposure, the measured noise was lower when the array was operated fluoroscopically than when operated radiographically, since it is in fluoroscopic mode that charge carryover has an effect. In fluoroscopic mode and at a given exposure, the measured noise was lower for decreased photodiode bias voltage due to increased effects of charge trapping and release. These observations are consistent with the discussion presented in Sec. III B 3.

D. Detective quantum efficiency

1. Zero-frequency detective quantum efficiency

The consistently good agreement between theoretical and empirical signal and noise results gives confidence that the system is modeled correctly and that the estimated gain, spreading, and noise parameters are accurate in describing the signal and noise performance of the imaging system. Using Eq. (20), calculations of the DQE(0) were performed for conditions corresponding to the three applications listed in
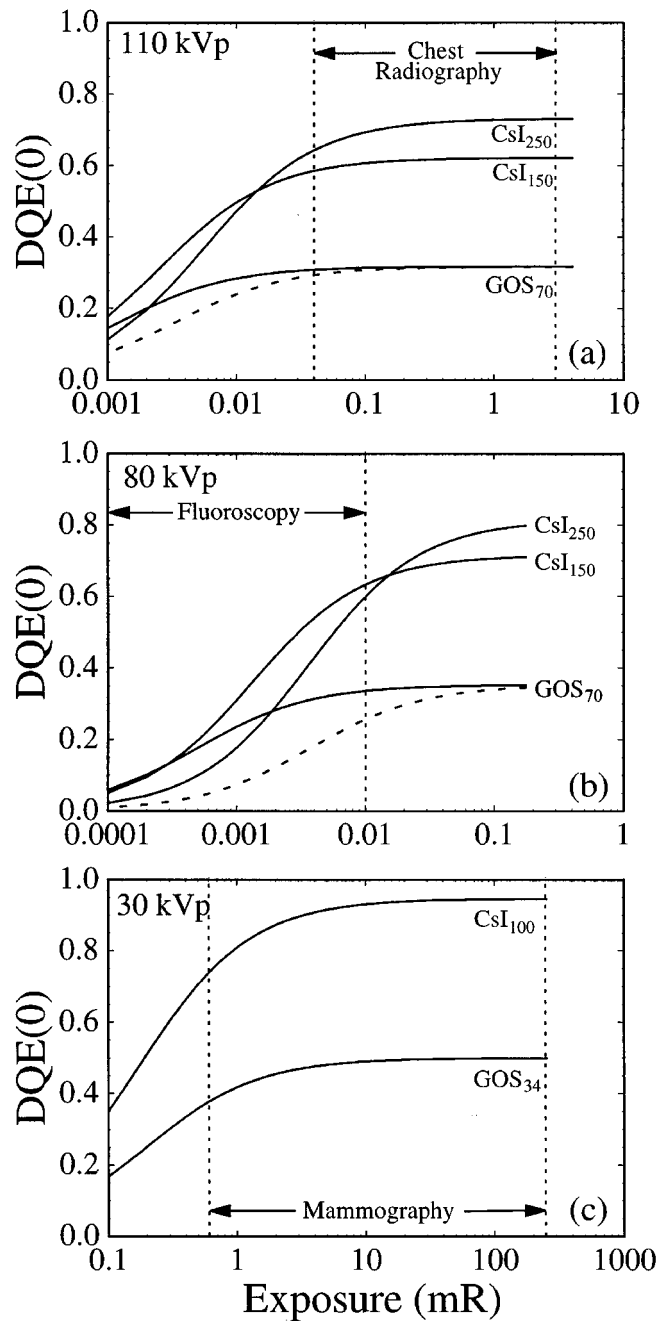

FIG. 8. Calculated DQE(0) vs exposure for a-Si:H imagers in (a) radiography, (b) fluoroscopy, and (c) mammography. The curves labeled "GOS$_{70}$," "GOS$_{34}$," "CsI$_{250}$," "CsI$_{150}$," and "CsI$_{100}$" correspond to imagers incorporating a Gd$_2$O$_2$S:Tb (70 or 34 mg/cm^2) or CsI:Tl (250, 150, or 100 mg/cm^2) x-ray converter, respectively. A nominal fill factor of 75% was assumed, and the intrinsic pixel noise was calculated using Eq. (9c). An additive amplifier noise of 1000 e was assumed. The dashed curve corresponds to the 127 μm pitch prototype array in combination with 70 mg/cm^2 Gd$_2$O$_2$S:Tb.

Table I for the specified pixel pitch and x-ray converters. In this way the relative importance of a wide range of system parameters was explored in terms of the effect upon DQE(0). Figures 8, 9, and 10 show the effect on DQE(0) of exposure level, additive amplifier noise, and fill factor, respectively.

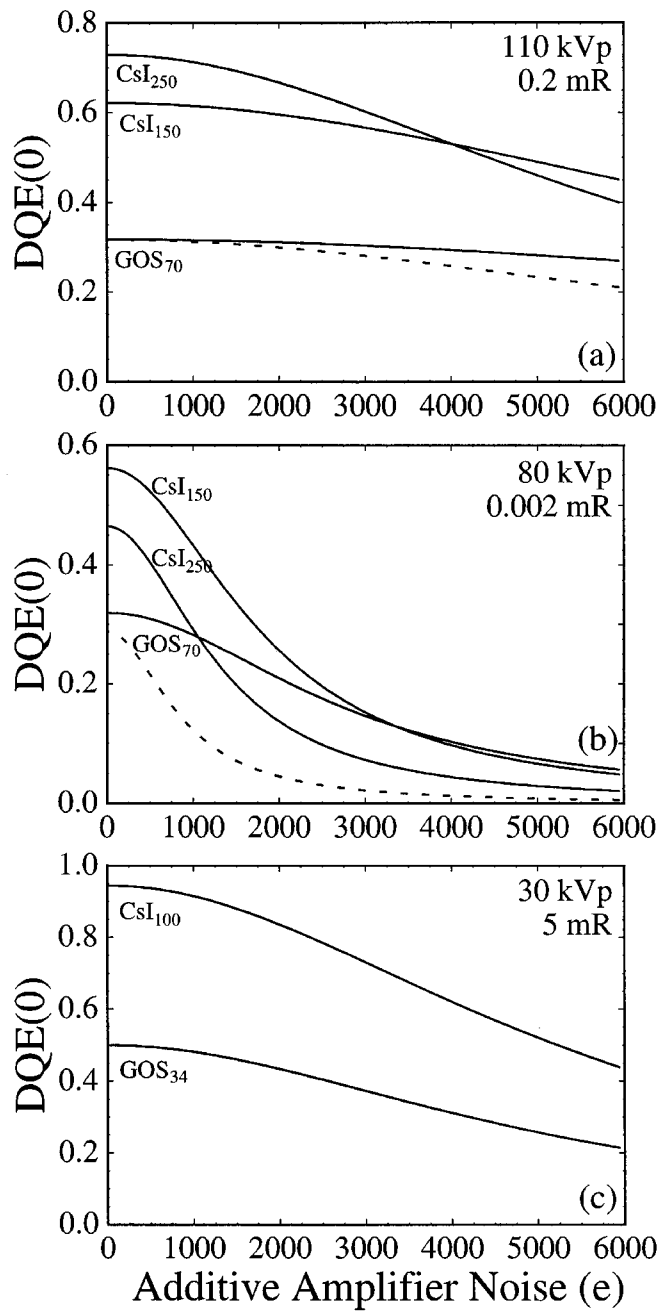*a. DQE(0): Effect of incident exposure level.* Figures

FIG. 9. Calculated DQE(0) vs additive amplifier noise for a-Si:H imagers in (a) radiography, (b) fluoroscopy, and (c) mammography at exposures corresponding approximately to the mean exposure to the detector for the application. The curves are labeled as in Fig. 8, and a nominal fill factor of 75% was assumed. The dashed curve corresponds to the 127 μm pitch prototype array in combination with 70 mg/cm^2 Gd$_2$O$_2$S:Tb.

FIG. 10. Calculated DQE(0) vs fill factor for a-Si:H imagers in (a) radiography, (b) fluoroscopy, and (c) mammography at exposures corresponding approximately to the mean exposure to the detector for each application. The curves are labeled as in Fig. 8, and amplifier noise of 1000 e was assumed.

8(a), 8(b), and 8(c) show the calculated DQE(0) versus exposure to the detector for conditions corresponding to radiography, fluoroscopy, and mammography, respectively. For each application, a typical range of clinical exposures is indicated by vertical dashed lines. The calculated DQE(0) for pixels in combination with CsI:Tl are generally higher than with Gd$_2$O$_2$S:Tb, because the CsI:Tl converters have higher quantum efficiency. In radiography [Fig. 8(a)], it is evident that the DQE(0) is limited primarily by the quantum effi-
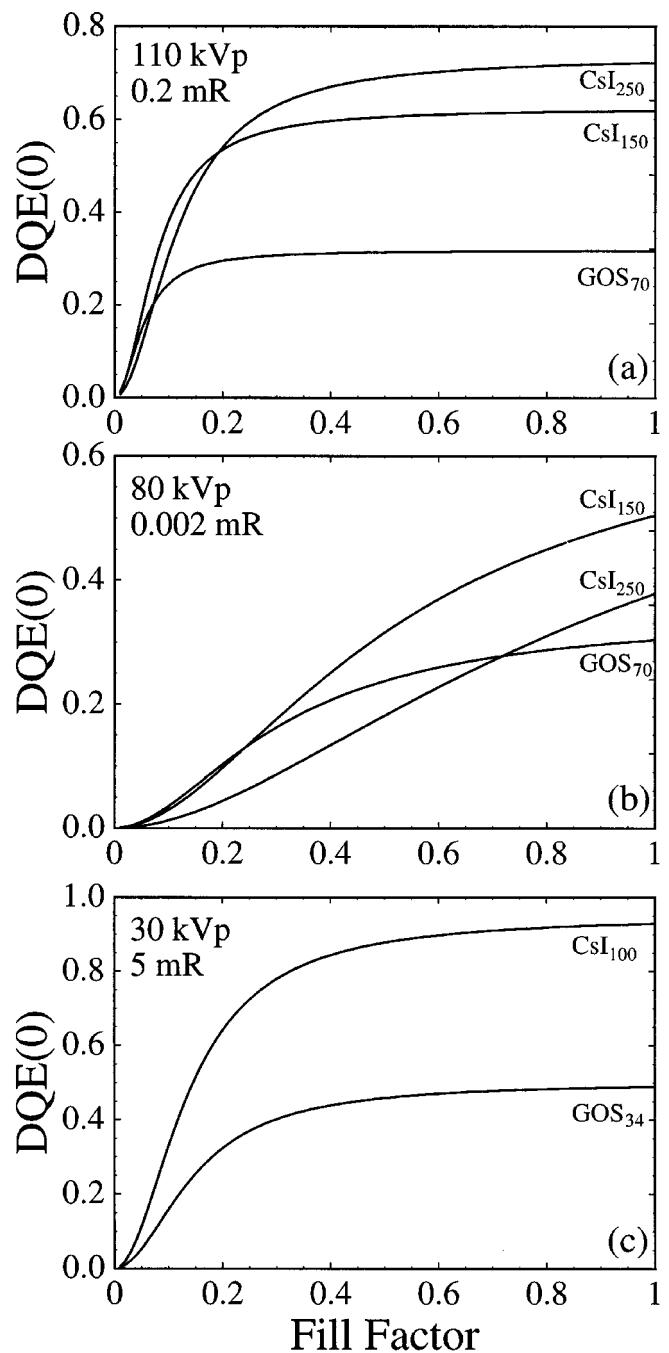
ciency and Poisson excess of the x-ray converter over the specified range.

Figure 8(b) shows the calculated DQE(0) under conditions corresponding to fluoroscopy. For the low exposures typical of this application, the DQE(0) depends strongly on the amount of incident radiation, and the quantum efficiency, quantum gain, and Poisson excess all have an appreciable effect on the DQE(0). Over the range of exposures relevant
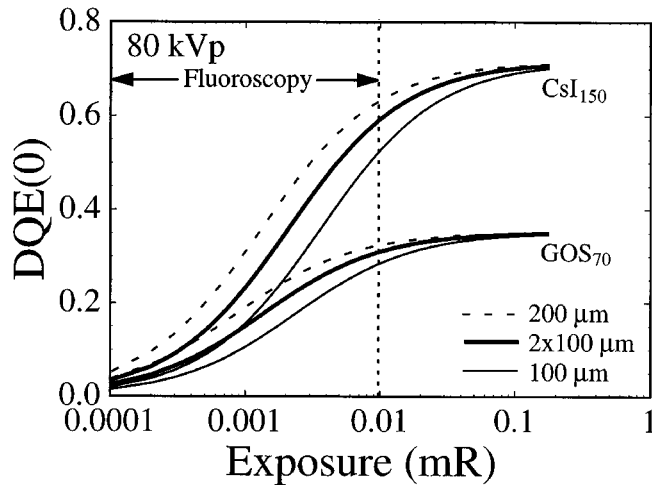
FIG. 11. DQE(0) vs exposure for different modes of fluoroscopic imaging. The curves labeled ''200 μm'' and ''100 μm'' correspond to ''full-resolution'' readout of a 200 μm pitch imager [as in Fig. 8(b)] and a 100 μm pitch imager, respectively, whereas the curves labeled ''2$\times$100 μm'' correspond to ''half-resolution'' readout of a 100 μm pitch imager.

to fluoroscopy, the 250 mg/cm^2 CsI:Tl screen gives poorer DQE(0) than the thinner, 150 mg/cm^2 screen due to the fact that although the thicker screen has improved quantum efficiency, it has lower quantum gain due to self-attenuation of optical quanta.[23] These calculations demonstrate the challenging nature of the fluoroscopic application, and optimized converters are likely essential in order to provide clinically acceptable imaging performance.

Figure 8(c) shows the calculated DQE(0) versus exposure for conditions relevant to mammography. For exposures above $\sim$10 mR, the DQE(0) is limited (as in radiography) primarily by the quantum efficiency and Poisson excess of the x-ray converter. Below $\sim$1 mR, however, the DQE(0) degrades rapidly with decreasing exposure (as in fluoroscopy).

b. DQE(0): Effect of additive amplifier noise. Figures 9(a), 9(b), and 9(c) show the effect of additive amplifier noise on the DQE(0). Plotting the DQE(0) in this manner allows examination of how additive noise degrades imager performance and suggests a means of identifying the maximum tolerable additive noise level for a given application. In radiography [Fig. 9(a)], the DQE(0) degrades slowly with increasing amplifier noise due to the high incident fluence and dominance of x-ray quantum noise.

In fluoroscopy [Fig. 9(b)], the DQE(0) degrades more rapidly with increasing amplifier noise due to the low incident fluence. The additive amplifier noise constrains the DQE(0) of the imager to values considerably less than that ultimately achievable unless the amplifier noise is reduced to levels below $\sim$1000 e. Once again, the challenging nature of the fluoroscopic application is evident.

Figure 9(c) shows the calculated DQE(0) versus additive amplifier noise for the case of mammography, where the mean exposure level is $\sim$2500 times greater than in fluoroscopy. Although there are considerably more incident quanta, the small pixel size necessary for high spatial resolution

tends to counter the benefit of increased exposure, and the effect of additive amplifier noise on the DQE(0) is somewhat stronger than in radiography and somewhat weaker than in fluoroscopy.

c. DQE(0): Effect of pixel fill factor. Figures 10(a), 10(b), and 10(c) show the effect of fill factor upon DQE(0). Figure 10(a) shows that in radiography, due to the relatively large incident fluence, there is little improvement in DQE(0) for fill factors above $\sim$0.3 for the selected converters. Under fluoroscopic conditions, however, where the incident fluence is small, increasing the fill factor has a more appreciable effect upon DQE(0), as shown in Fig. 10(b). Finally, Fig. 10(c) shows that in mammography, where the incident fluence is relatively high but the pixel pitch is small, there is considerable improvement in DQE(0) with increasing fill factors up to $\sim$0.5, above which the DQE(0) improves only marginally.

2. "Full-resolution" and "half-resolution" digital radiography and fluoroscopy

In many fluoroscopic applications, it is common to interrupt the fluoroscopic sequence momentarily in order to obtain a high quality radiograph (e.g., spot film) and then continue the fluoroscopic sequence. The fact that *a*-Si:H imagers can be operated both radiographically and fluoroscopically suggests an interesting and potentially valuable means of operating these devices. A 100 μm pitch array (suitable for radiography) could be operated fluoroscopically at ''half-resolution'' by addressing pairs of gate lines simultaneously. The half-resolution mode reduces the spatial resolution in one direction but automatically provides higher frame rate (without compromising amplifier bandwidth or ADC resolution), and the imager could be switched to full-resolution mode in order to acquire a high quality (digital spot) radiograph. In half-resolution mode, the effective pixel area is doubled, but the additive pixel noise is increased by $\sqrt{2}$. [An alternative way of handling image data may be considered wherein pairs of gate lines are simultaneously addressed *and* the signal from adjacent data lines are combined after amplification. Such a mode of operation effectively quadruples the pixel area, reduces the spatial resolution in both the *x* and *y* directions, and increases the pixel and amplifier noise by $\sqrt{4}$ and $\sqrt{2}$, respectively. Examination of Eq. (20) reveals, however, that this alternative mode of readout (half-resolution in both *x* and *y* directions) yields DQE(0) equivalent to that for the half-resolution mode (one direction only) described above. For purposes of discussion, only the half-resolution mode (one direction) is considered.] Therefore, considering only the pixel and amplifier noise components of the additive noise,

$$\sigma_{\text{add}}^2 \approx \sigma_{\text{pix}}^2 + \sigma_{\text{amp}}^2 \quad \text{(full-resolution mode),} \tag{21a}$$

and

$$\sigma_{\text{add}}^2 \approx 2\sigma_{\text{pix}}^2 + \sigma_{\text{amp}}^2 \quad \text{(half-resolution mode).} \tag{21b}$$

The tradeoff between increased pixel area and increased additive noise is such that the net effect is an improved (zero-

frequency) signal-to-noise ratio. The full-resolution performance of 100 μm pitch imagers under radiographic conditions is as discussed above [Figs. 8(a), 9(a), and 10(a)], and that for 200 μm pitch imagers under fluoroscopic conditions is as shown in Figs. 8(b), 9(b), and 10(b). The DQE(0) for a 100 μm pitch imager operated in half-resolution mode can be similarly calculated using Eqs. (20) and (21b).

Figure 11 shows the DQE(0) versus exposure for 100 μm pitch imagers in half-resolution mode in comparison to full-resolution operation of 100 and 200 μm pitch imagers under fluoroscopic conditions. The nominal parameters assumed in the calculations are the same as in Fig. 8(b). The three curves for each configuration correspond to full- and half-resolution modes of operation for arrays with different pixel pitch. The half-resolution case (''2×100 μm'') shows improved DQE(0) compared to full-resolution operation of the same array (''100 μm'') and approaches the ''200 μm'' case. This analysis is useful, since it describes the extent to which the same 100 μm pitch imager could be used for both (half-resolution) fluoroscopy and (full-resolution) radiography by switching between two modes of readout.

V. DISCUSSION AND CONCLUSIONS

Cascaded systems modeling provides a useful means of characterizing the signal and noise properties of a-Si:H imaging systems. Sufficiently general to describe a wide range of imager configurations and exposure conditions, the model has been used to analyze the performance of existing systems and to explore the potential performance of hypothetical imaging systems.

The model describes the signal characteristics of the 127 μm pitch imager with reasonable accuracy as demonstrated by the agreement between theoretical and empirical x-ray sensitivity (Fig. 6). The model is quite robust in this regard, giving good agreement between theory and measurement for a wide range of energies, x-ray converters, modes of operation, and array designs. Similarly, the model accurately describes the empirical individual pixel noise, accounting for effects such as image blur, image lag, and signal nonlinearity (Fig. 7). The good agreement between theoretical and empirical signal and noise supports the hypothesis that the model can be used to predict properties such as DQE.

A powerful incentive for the development of theoretical models describing the signal and noise properties of an imaging system is to allow an examination of the potential performance of hypothetical systems. With the cascaded systems model presented in this paper, an initial theoretical investigation of the DQE(0) performance of a-Si:H imaging technology in radiography, fluoroscopy, and mammography has been reported (Figs. 8–11). Although the results are restricted to zero frequency, they nevertheless demonstrate many important considerations. In radiography, the DQE(0) is limited primarily by the quantum efficiency of the x-ray converter and suggests that a-Si:H imagers could provide imaging performance comparable or superior to existing screen-film and computed radiography systems. For ex-

ample, the DQE(0) for an a-Si:H imager employing a Lanex Regular converter is comparable to that measured for screen-film[57,58] and computed radiography[59] systems, and the DQE(0) for an a-Si:H imager employing CsI:Tl is considerably higher. Furthermore, since CsI:Tl converters can be fabricated in columnar structures which help reduce the spread of optical quanta, such channeled-light converters can be made quite thick (to improve the quantum efficiency) without gross reduction of MTF. To realize the potential of AM-FPIs incorporating channeled CsI:Tl converters, however, technical issues such as uniformity over large area remain to be resolved.

Fluoroscopy represents a more challenging application for indirect detection AMFPIs due to the relatively low number of input x-ray quanta per frame. Although the DQE(0) is ultimately limited by the quantum efficiency of the x-ray converter at high exposures, the calculations predict that the DQE(0) for a-Si:H imagers, as modeled, is constrained by system parameters such as quantum gain, fill factor, and additive noise at low exposures. The DQE reported for commercial XRIIs[23,55,60] suggests that such fluoroscopic imagers are limited by the quantum efficiency of the input phosphor (at the selected exposures), and it remains to be seen whether fully optimized flat-panel imagers can provide comparable performance. Indirect detection AMFPIs possess a number of pertinent advantages over XRIIs, such as thin profile and absence of image distortion and glare, and development of higher fill factor arrays and low-noise amplifiers would certainly augment their application in fluoroscopy. Furthermore, the possibility of using a single (e.g., 100 μm pitch) imager for both radiography and fluoroscopy as described in Sec. IV D 2 presents a potentially promising aspect of the technology, especially in environments where the imaging task routinely and rapidly switches between real-time fluoroscopy and radiography (e.g., spot film). Furthermore, the imagers could provide high-resolution fluoroscopy of regions of interest using a ''digital zoom''[5] in which a portion of the array is addressed at high frame rate and full resolution.

Finally, full-field mammography represents a potential field of application for a-Si:H imagers, and the DQE(0) calculated for a hypothetical, 50 μm pitch imager is comparable or superior to existing screen-film and CCD-based imagers.[61,62] However, a number of design issues remain to be explored before clinically useful a-Si:H imagers can be developed for mammography. For example, there is a necessary tradeoff between pixel pitch and fill factor for arrays incorporating a discrete photodiode design.[63] A potential solution is to develop arrays incorporating a continuous photodiode design.[63,64] Such arrays could provide sufficiently fine pixel pitch with fill factor near unity, although charge sharing between neighboring pixels may result in reduced pixel MTF.[63] As in fluoroscopy, development of low-noise amplifiers represents a beneficial and perhaps necessary step toward the application of such imagers and is the subject of ongoing research.

Cascaded systems modeling provides a tool for exploring imager optimization by examining the effect of varying the system parameters upon DQE. By exploring the achievable

parameters in an iterative fashion, an imager configuration which maximizes DQE for a given set of exposure conditions and imaging task can be determined. This allows one to estimate the performance of an imager configuration before committing time and expense to actual construction. For example, the important tradeoffs between quantum efficiency, quantum gain, Poisson excess, and MTF of the converter can be explored in terms of the effect upon system DQE. Similarly, the relative effect of pixel pitch, fill factor, and additive electronic noise upon DQE can be investigated. Of course, it is the spatial frequency-dependent DQE which should be considered in system optimization in order to account for the spatial effects (e.g., blurring or aliasing) of varying the system parameters. Measurement of the spatial frequency-dependent signal and noise properties of a-Si:H imagers and comparison to theoretical results are underway.

The general model reported in this paper could be used to describe the imaging properties of a wide variety of indirect detection AMFPIs. Empirical and theoretical results have been shown for an array with pixels consisting of a photodiode in combination with a TFT (photodiode+TFT), but the general model could also apply to array designs which incorporate a photodiode+single[2,65,66] or dual[67] diode, or a phototransistor+TFT[68] as well as those which employ a continuous photodiode layer.[63] The general system parameters represented in the QAD of Fig. 3 could characterize the performance of these systems, with the additive electronic noise for a given system represented by a single, general term, σ^2_{add}. A modified cascaded systems model could be applied to imagers which detect incident x rays directly, such as those employing a continuous photoconductive layer.[4,69] The generality of the theoretical approach therefore provides not only a means of predicting and optimizing the performance of a given system, but it also provides an objective means of comparing the potential performance of different imaging systems.

ACKNOWLEDGMENTS

APPENDIX A: NOISE POWER SPECTRUM

Using Eqs. (2a), (2b), and (2c), the NPS at the output of each stage in the QAD can be calculated,

$$S_1(u,v) = \bar{g}_1^2 S_0(u,v) + \bar{q}_0 \bar{g}_1(1-\bar{g}_1) = \bar{q}_0 \bar{g}_1,$$
$$S_2(u,v) = \bar{g}_2^2 S_1(u,v) + \bar{g}_1 \sigma_{g_2}^2 \bar{q}_0. \tag{A1}$$

Writing the gain-variance in terms of the Poisson excess gives

$$S_2(u,v) = \bar{q}_0 \bar{g}_1 \bar{g}_2 (\bar{g}_2 + 1 + \epsilon_{g_2}), \tag{A2}$$

$$\begin{aligned}
S_3(u,v) &= (S_2(u,v) - \bar{q}_0 \bar{g}_1 \bar{g}_2) T_3^2(u,v) + \bar{q}_0 \bar{g}_1 \bar{g}_2 \\
&= [\bar{q}_0 \bar{g}_1 \bar{g}_2 (\bar{g}_2 + 1 + \epsilon_{g_2}) - \bar{q}_0 \bar{g}_1 \bar{g}_2] T_3^2(u,v) \\
&\quad + \bar{q}_0 \bar{g}_1 \bar{g}_2 \\
&= \bar{q}_0 \bar{g}_1 \bar{g}_2 [1 + (\bar{g}_2 + \epsilon_{g_2}) T_3^2(u,v)], \tag{A3}
\end{aligned}$$

$$\begin{aligned}
S_4(u,v) &= \bar{g}_4^2 S_3(u,v) + \bar{q}_0 \bar{g}_1 \bar{g}_2 \bar{g}_4 (1-\bar{g}_4) \\
&= \bar{q}_0 \bar{g}_4^2 \bar{g}_1 \bar{g}_2 [1 + (\bar{g}_2 + \epsilon_{g_2}) T_3^2(u,v)] \\
&\quad + \bar{q}_0 \bar{g}_1 \bar{g}_2 \bar{g}_4 (1-\bar{g}_4) \\
&= \bar{q}_0 \bar{g}_1 \bar{g}_2 \bar{g}_4 [1 + \bar{g}_4 (\bar{g}_2 + \epsilon_{g_2}) T_3^2(u,v)]. \tag{A4}
\end{aligned}$$

Finally, for the presampling NPS at stage 5 of the imaging chain, we have

$$\begin{aligned}
S_5(u,v) &= S_4(u,v) a_{pd}^4 T_5^2(u,v) + S_{add}(u,v) \\
&= a_{pd}^4 \bar{q}_0 \bar{g}_1 \bar{g}_2 \bar{g}_4 [1 + \bar{g}_4 (\bar{g}_2 + \epsilon_{g_2}) T_3^2(u,v)] \\
&\quad \times T_5^2(u,v) + S_{add}(u,v), \tag{A5}
\end{aligned}$$

where a square photodiode with a sampling aperture of a_{pd} is assumed.

APPENDIX B: INDIVIDUAL PIXEL NOISE

The variance in pixel signal at stage 5 of the imaging chain is given by the integral of $S_5(u,v)$ over the frequency domain:

$$\begin{aligned}
\sigma_{N_5}^2 &= \int_{-\infty}^{+\infty} \int_{-\infty}^{+\infty} S_5(u,v) du\,dv \\
&= a_{pd}^4 \bar{q}_0 \bar{g}_1 \bar{g}_2 \bar{g}_4 \int_{-\infty}^{+\infty} \int_{-\infty}^{+\infty} [1 + \bar{g}_4(\bar{g}_2 + \epsilon_{g_2}) T_3^2(u,v)] \\
&\quad \times T_5^2(u,v) du\,dv + \int_{-\infty}^{+\infty} \int_{-\infty}^{+\infty} S_{add}(u,v) du\,dv \\
&= a_{pd}^4 \bar{q}_0 \bar{g}_1 \bar{g}_2 \bar{g}_4 \left[\int_{-\infty}^{+\infty} \int_{-\infty}^{+\infty} T_5^2(u,v) du\,dv + \bar{g}_4(\bar{g}_2 + \epsilon_{g_2}) \right. \\
&\quad \left. \times \int_{-\infty}^{+\infty} \int_{-\infty}^{+\infty} T_3^2(u,v) T_5^2(u,v) du\,dv \right] + \sigma_{add}^2.
\end{aligned}$$

Assuming a square photodiode, the pixel MTF may be approximated by a sinc function:[10]

$$T_5(u,v) = |\text{sinc}(a_{pd}u) \text{sinc}(a_{pd}v)| \tag{B1}$$

so that

$$\int_{-\infty}^{+\infty} \int T_5^2(u,v) du\,dv = \frac{1}{a_{pd}^2}. \tag{B2}$$

Therefore, the variance can be written as

$$\sigma_{N_5}^2 = a_{\text{pd}}^2 \bar{q}_0 \bar{g}_1 \bar{g}_2 \bar{g}_4 \left[1 + \bar{g}_4(\bar{g}_2 + \epsilon_{g_2}) a_{\text{pd}}^2 \right.$$

$$\left. \times \int_{-\infty}^{+\infty} \int T_3^2(u,\nu) T_5^2(u,\nu) du d\nu \right] + \sigma_{\text{add}}^2.$$

It is convenient to define a ''sharpness factor,'' s:

$$s \equiv a_{\text{pd}}^2 \int_{-\infty}^{+\infty} \int T_3^2(u,\nu) T_5^2(u,\nu) du d\nu, \tag{B3}$$

which depends on the MTFs of the converting screen and the photodiode. Note that the sharpness factor has values $0 \leq s \leq 1$, where s is unity for the case of an ideal converter [i.e., for $T_3(u,\nu) = 1$]. The relation for the individual pixel variance therefore reduces to

$$\sigma_{N_5}^2 = a_{\text{pd}}^2 \bar{q}_0 \bar{g}_1 \bar{g}_2 \bar{g}_4 [1 + \bar{g}_4(\bar{g}_2 + \epsilon_{g_2}) s] + \sigma_{\text{add}}^2. \tag{B4}$$

APPENDIX C: THE EFFECT OF CHARGE CARRYOVER ON INDIVIDUAL PIXEL NOISE

When the imager is operated in fluoroscopic mode, charge carryover affects the individual pixel noise by correlating information between frames. A deterministic model similar to that reported by Matsunaga *et al.*[44] relates the pixel variance with the fraction of trapped charge, t. The parameters of interest are shown schematically in Fig. 5 and described in Sec. III B 3. The model is deterministic in that it considers the magnitude of t to be constant for a given set of operating conditions and does not account for possible fluctuations in this parameter. Such fluctuations are assumed negligible, and the analysis below illustrates the effect of charge carryover on individual pixel noise.

The amount of charge available for readout from the $(n+1)$th frame is

$$Q_{(n+1)} = G_{(n+1)} + N_{\text{int}(n+1)} + (Q_{(n)} - R_{(n)}). \tag{C1}$$

Since the external noise source $[N_{\text{ext}(n)}]$ is not affected by the charge trapping mechanism, the associated variance, $\sigma_{N_{\text{ext}(n)}}^2$, will be independent of the parameter t. Therefore, the term $N_{\text{ext}(n)}$ can be ignored in the following derivation, and the variance $\sigma_{N_{\text{ext}(n)}}^2$ will be added in quadrature with the result. Therefore, the charge read out of the pixel (ignoring the external noise source) is

$$R_{(n)} = (1-t) Q_{(n)}. \tag{C2}$$

The system is assumed to be in signal equilibrium, so that $\overline{Q_{(n)}^2} = \overline{Q_{(n+1)}^2}$ and $\overline{R_{(n)}^2} = \overline{R_{(n+1)}^2}$. Furthermore, the quantities $G_{(n+1)}, Q_{(n)}, N_{\text{int}(n)},$ and $N_{\text{ext}(n)}$ are assumed to be independent ($\overline{G_{(n)} Q_{(n)}} = \overline{G_{(n)}}\, \overline{Q_{(n)}}$, etc.), and $N_{\text{int}(n)}$ and $N_{\text{ext}(n)}$ have zero mean ($\overline{N_{\text{int}(n)}} = \overline{N_{\text{ext}(n)}} = 0$). For a general variable, X, the variance can be written as

$$\sigma_X^2 = \overline{X^2} - \overline{X}^2. \tag{C3}$$

Therefore the variance in signal read from individual pixels is

$$\sigma_{R_{(n)}}^2 = \overline{R_{(n)}^2} - \overline{R_{(n)}}^2.$$

The purpose of the following derivation is to determine this variance as a function of the parameter t. Equation (C2) implies

$$\overline{R_{(n)}} = (1-t) \overline{Q_{(n)}},$$

$$\overline{R_{(n)}^2} = (1-t)^2 \overline{Q_{(n)}^2}.$$

Therefore, the pixel variance may be written as

$$\sigma_{R_{(n)}}^2 = (1-t)^2 \overline{Q_{(n)}^2} - \overline{R_{(n)}}^2. \tag{C4}$$

To find $\overline{Q_{(n)}^2}$, we first consider Eq. (C1),

$$\overline{Q_{(n+1)}} = \overline{G_{(n+1)}} + \overline{N_{\text{int}(n+1)}} + \overline{Q_{(n)}} - \overline{R_{(n)}}$$

$$= \overline{G_{(n+1)}} + \overline{Q_{(n)}} - \overline{R_{(n)}},$$

which implies

$$\overline{R_{(n)}} = \overline{G_{(n+1)}}$$

for a system in signal equilibrium. To find $\overline{Q_{(n)}^2}$, we again use Eq. (C1) and write

$$\overline{Q_{(n+1)}^2} = \overline{G_{(n+1)}^2} + 2\overline{G_{(n+1)}}\,\overline{N_{\text{int}(n+1)}} + 2\overline{G_{(n+1)}}\,\overline{Q_{(n)}}$$

$$- 2\overline{G_{(n+1)}}\,\overline{R_{(n)}} + \overline{N_{\text{int}(n+1)}^2} + 2\overline{N_{\text{int}(n+1)}}\,\overline{Q_{(n)}}$$

$$- 2\overline{N_{\text{int}(n+1)}}\,\overline{R_{(n)}} + \overline{Q_{(n)}^2} - 2\overline{R_{(n)}}\,\overline{Q_{(n)}} + \overline{R_{(n)}^2}$$

$$= \overline{G_{(n+1)}^2} + 2\overline{G_{(n+1)}}\,\overline{Q_{(n)}} - 2\overline{G_{(n+1)}}\,\overline{R_{(n)}}$$

$$+ \overline{N_{\text{int}(n+1)}^2} + \overline{Q_{(n)}^2} - 2\overline{R_{(n)}}\,\overline{Q_{(n)}} + \overline{R_{(n)}^2}.$$

Using Eq. (C2), this expression may be written explicitly in terms of the factor t. Assuming signal equilibrium and using Eqs. (C2) and (C3) again yields

$$\overline{Q_{(n)}^2} = \overline{G_{(n+1)}^2} + 2t\overline{G_{(n+1)}}\,\overline{Q_{(n)}} + \overline{N_{\text{int}(n+1)}^2} + t^2 \overline{Q_{(n)}^2}$$

$$= \frac{1}{1-t^2} (\overline{G_{(n+1)}^2} + 2t\overline{G_{(n+1)}}\,\overline{Q_{(n)}} + \overline{N_{\text{int}(n+1)}^2})$$

$$= \frac{\sigma_{G_{(n)}}^2}{(1-t)(1+t)} + \frac{\overline{N_{\text{int}(n+1)}^2}}{(1-t)(1+t)} + \frac{\overline{R_{(n)}}^2}{(1-t)^2}.$$

Substituting this into Eq. (C4) for the variance yields

$$\sigma_{R_{(n)}}^2 = \left(\frac{1-t}{1+t} \right) (\sigma_{G_{(n)}}^2 + \overline{N_{\text{int}(n+1)}^2}) + \overline{R_{(n)}}^2 - \overline{R_{(n)}}^2$$

$$= \left(\frac{1-t}{1+t} \right) (\sigma_{G_{(n)}}^2 + \overline{N_{\text{int}(n+1)}^2}).$$

Finally, the variance, $\sigma_{N_{\text{ext}(n)}}^2$, due to independent external noise sources can be added to the result, and since

$$\overline{N_{\text{int}(n+1)}^2} = \sigma_{N_{\text{int}(n+1)}}^2 + \overline{N_{\text{int}(n+1)}}^2 = \sigma_{N_{\text{int}(n+1)}}^2,$$

the pixel variance may be written as

$$\sigma_{R_{(n)}}^2 = \left(\frac{1-t}{1+t} \right) (\sigma_{G_{(n)}}^2 + \sigma_{N_{\text{int}(n)}}^2) + \sigma_{N_{\text{ext}(n)}}^2. \tag{C5}$$

In the limit of zero lag ($t=0$) Eq. (C5) is equivalent to Eq. (12). In the case of nonzero lag, however, the pixel variance is suppressed due to charge carryover between frames. As shown in Refs. 5 and 28, the parameter t is a function of applied photodiode bias voltage and signal level.

[1] U. W. Schiebel, N. Conrads, N. Jung, M. Weibrecht, H. Wieczorek, T. T. Zaengel, M. J. Powell, I. D. French, and C. Glasse, ''Fluoroscopic x-ray imaging with amorphous silicon thin-film arrays,'' Proc. SPIE **2163**, 129–140 (1994).

[2] J. Chabbal, C. Chaussat, T. Ducourant, L. Fritsch, J. Michailos, V. Spinnler, G. Vieux, M. Arques, G. Hahm, M. Hoheizel, H. Horbachek, R. Schulz, and M. Spahn, ''Amorphous silicon x-ray image sensor,'' Proc. SPIE **2708**, 499–510 (1996).

[3] S. Ross, I. Naday, M. Kanyo, M. L. Westbrook, E. M. Westbrook, W. C. Phillips, M. J. Stanton, and R. A. Street, ''Amorphous silicon area detectors for protein crystallography,'' Proc. SPIE **2415**, 189–203 (1995).

[4] W. Zhao and J. A. Rowlands, ''X-ray imaging using amorphous selenium: Feasibility of a flat panel self-scanned detector digital radiology,'' Med. Phys. **22**, 1595–1604 (1995).

[5] L. E. Antonuk, Y. El-Mohri, J. H. Siewerdsen, J. Yorkston, W. Huang, and V. E. Scarpine, ''Empirical investigation of the signal performance of a high-resolution, indirect detection, active matrix flat panel imager (AM-FPI) for diagnostic radiology,'' Med. Phys. **24**, 51–70 (1997).

[6] J. P. Bissonette, I. A. Cunningham, D. A. Jaffray, A. Fenster, and P. Munro, ''A quantum accounting and detective quantum efficiency analysis for video-based portal imaging,'' Med. Phys. (submitted).

[7] G. Spekowius, H. Boerner, W. Eckenbach, P. Quadflieg, and G. J. Laurenssen, ''Simulation of the imaging performance of x-ray image intensifier/TV camera chains,'' Proc. SPIE **2432**, 12–23 (1995).

[8] H. H. Barrett and W. S. Swindell, *Radiological Imaging: The Theory of Image Formation, Detection and Processing* (Academic, New York, 1981).

[9] M. Rabbani, R. Shaw, and R. Van Metter, ''Detective quantum efficiency of imaging systems with amplifying and scattering mechanisms,'' J. Opt. Soc. Am. A **4**, 895–901 (1987).

[10] J. C. Dainty and R. Shaw, *Image Science: Principles, Analysis and Evaluation of Photograhic-type Imaging Processes* (Academic, London, 1974).

[11] I. A. Cunningham, M. S. Westmore, and A. Fenster, ''A spatial-frequency dependent quantum accounting diagram and detective quantum efficiency model of signal and noise propagation in cascaded imaging systems,'' Med. Phys. **21**, 417–427 (1994).

[12] I. A. Cunningham, M. S. Westmore, and A. Fenster, ''Unification of image blur and noise using a stochastic convolution operator,'' Med. Phys. (to be published).

[13] R. K. Swank, ''Absorption and noise in x-ray phosphors,'' J. Appl. Phys. **44**, 4199–4203 (1973).

[14] R. N. Bracewell, *The Fourier Transform and its Applications* (McGraw-Hill, New York, 1986).

[15] I. A. Cunningham, M. S. Westmore, and A. Fenster, ''Visual impact of the non-zero spatial frequency quantum sink,'' Proc. SPIE **2163**, 274–283 (1994).

[16] M. S. Westmore and I. A. Cunningham, ''Analysis of the detective quantum efficiency of coupling a CCD to a scintillating phosphor for x-ray microtomographic imaging,'' Proc. SPIE **1896**, 82–92 (1993).

[17] A. D. A. Maidment and M. J. Yaffe, ''Analysis of the spatial-frequency-dependent DQE of optically coupled digital mammography detectors,'' Med. Phys. **21**, 721–729 (1994).

[18] J. H. Siewerdsen, L. E. Antonuk, and J. Yorkston, ''Theoretical performance of amorphous silicon imagers in diagnostic radiology,'' Proc. SPIE **2708**, 484–493 (1996).

[19] H. E. Johns and J. R. Cunningham, *The Physics of Radiology* (Thomas, Springfield, 1983).

[20] D. P. Trauernicht and R. Van Metter, ''The measurement of conversion noise in x-ray intensifying screens,'' Proc. SPIE **914**, 100–116 (1988).

[21] D. P. Trauernicht and R. Van Metter, ''Conversion noise measurement for front and back x-ray intensifying screens,'' Proc. SPIE **1231**, 262–270 (1990).

[22] J. A. Rowlands and K. W. Taylor, ''Absorption and noise in cesium iodide x-ray image intensifiers,'' Med. Phys. **10**, 786–795 (1983).

[23] W. Hillen, W. Eckenbach, P. Quadflieg, and P. Zaengel, ''Signal-to-noise performance in cesium iodide x-ray fluorescent screens,'' Proc. SPIE **1443**, 120–131 (1991).

[24] A. Ginzburg and C. E. Dick, ''Image information transfer properties of x-ray intensifying screens in the energy range from 17 to 320 keV,'' Med. Phys. **20**, 1013–1021 (1993).

[25] R. M. Nishikawa, M. J. Yaffe, and R. B. Holmes, ''Effect of finite phosphor thickness on detective quantum efficiency,'' Med. Phys. **16**, 773–780 (1989).

[26] L. E. Antonuk, J. Yorkston, W. Huang, J. Boudry, and E. J. Morton, ''Radiation response characteristics of amorphous silicon arrays for megavoltage radiotherapy imaging,'' IEEE Trans. Nucl. Sci. **39**, 1069–1073 (1992).

[27] R. A. Street, *Hydrogenated Amorphous Silicon* (Cambridge University Press, New York, 1991).

[28] L. E. Antonuk, J. Yorkston, W. Huang, J. Boudry, E. J. Morton, M. J. Longo, and R. A. Street, ''Factors affecting image quality for megavoltage and diagnostic x-ray a-Si:H imaging arrays,'' Mater. Res. Soc. Symp. Proc. **258**, 1069–1074 (1992).

[29] J. Yorkston, L. E. Antonuk, N. Seraji, W. Huang, J. Siewerdsen, and Y. El-Mohri, ''Evaluation of the MTF for a-Si:H imaging arrays,'' Proc. SPIE **2163**, 141–148 (1994).

[30] J. Yorkston, L. E. Antonuk, N. Seraji, W. Huang, J. Siewerdsen, and Y. El-Mohri, ''MTF measurements with high resolution a-Si:H imaging arrays,'' Proc. SPIE **2432**, 260–269 (1995).

[31] M. L. Giger, K. Doi, and C. E. Metz, ''Investigation of basic imaging properties in digital radiography. Noise Wiener spectrum,'' Med. Phys. **11**, 797–805 (1984).

[32] J. M. Boudry, ''Evaluation of hydrogenated amorphous silicon photodiodes and field-effect transistors for use as elements of two-dimensional x-ray imaging arrays,'' Ph. D. thesis, University of Michigan, 1996.

[33] J. M. Boudry and L. E. Antonuk, ''Current-noise-power-spectra for amorphous silicon photodiode sensors,'' Mater. Res. Soc. Symp. Proc. **297**, 975–980 (1993).

[34] J. M. Boudry and L. E. Antonuk, ''Current-noise-power-spectra for amorphous silicon thin-film transistors,'' J. Appl. Phys. **76**, 2529–2534 (1994).

[35] R. G. Brown, *Introduction to Random Signal Analysis and Kalman Filtering* (Wiley, New York, 1983), Chap. 3.

[36] L. E. Antonuk, J. Yorkston, W. Huang, J. Siewerdsen, and R. A. Street, ''Considerations for high frame rate operation of two-dimensional a-Si:H imaging arrays,'' Mater. Res. Soc. Symp. Proc. **297**, 945–950 (1993).

[37] L. E. Antonuk, J. M. Boudry, Y. El-Mohri, W. Huang, J. H. Siewerdsen, J. Yorkston, and R. A. Street, ''Large area, flat-panel amorphous silicon imagers,'' Proc. SPIE **2432**, 216–227 (1995).

[38] C. D. Motchenbacher and F. C. Fitchen, *Low-Noise Electronic Design* (Wiley, New York, 1973).

[39] B. A. Widrow, ''A study of rough amplitude quantization by means of nyquist sampling theory,'' Proc. IRE Trans. Circuit Theory **PGCT-3**, 266–276 (1956).

[40] G. T. Barnes, ''Noise analysis of radiographic imaging,'' in *Recent Developments in Digital Imaging*, edited by K. Doi, L. Lanzl, and P. P. Lin (AIP, New York, 1985), pp. 16–38.

[41] R. W. Ramirez, *The FFT Fundamentals and Concepts* (Prentice-Hall, Englewood Cliffs, NJ, 1991).

[42] J. Yorkston, L. E. Antonuk, W. Huang, and R. A. Street, ''Photoresponse linearity of a-Si:H imaging pixels,'' Mater. Res. Soc. Symp. Proc. **297**, 951–956 (1993).

[43] G. Murphy, W. Bitler, J. Coffin, and R. Langdon, ''Lag vs. noise in fluoroscopic imaging,'' Proc. SPIE **1896**, 174–179 (1993).

[44] Y. Matsunaga, F. Hatori, T. Hiroyuki, and O. Yoshida, ''Analysis of signal to noise ratio of photoconductive layered solid-state imaging device,'' IEEE Trans. Electron Devices **42**, 38–42 (1995).

[45] L. E. Antonuk, J. H. Siewerdsen, J. Yorkston, and W. Huang, ''Radiation response of amorphous silicon imaging arrays at diagnostic energies,'' IEEE Trans. Nucl. Sci. **14**, 1500–1505 (1994).

[46] P. R. Bevington and D. K. Robinson, *Data Reduction and Error Analysis for the Physical Sciences*, 2nd ed. (McGraw-Hill, New York, 1992).

[47] R. Birch, M. Marshall, and G. M. Ardran, ''Catalogue of spectral data for diagnostic x-rays,'' Hospital Physicists' Association, Scientific Report Series 30 (1979).

[48] E. Storm and H. I. Israel, ''Photon cross sections from 1 keV to 100 MeV for elements $Z=1$ to $Z=100$,'' Nucl. Data Tables **A7**, 565–681 (1970).

[49] M. J. Flynn, S. M. Hames, and J. J. Ciarelli, ''The effect of direct x-ray

interaction in the photodetector on image noise for a CCD/scintillator system,'' Proc. SPIE **2708**, 116–127 (1996).

[50]T. S. Curry III, J. E. Dowdey, and R. C. Murry, *Christensen's Physics of Diagnostic Radiology* (Lea & Febiger, Philadelphia, 1990).

[51]C. E. Metz, R. F. Wagner, K. Doi, D. G. Brown, R. M. Nishikawa, and K. J. Myers, ''Toward consensus on quantitative assessment of medical imaging systems,'' Med. Phys. **22**, 1057–1061 (1995).

[52]T. R. Fewell and R. E. Shuping, ''Handbook of mammographic x-ray spectra,'' U.S. Department of Health, Education, and Welfare (1978).

[53]F. G. Rueter, B. J. Conway, J. L. McCrohan, and O. H. Suleiman, ''Average radiation exposure values for three diagnostic radiographic examinations,'' Radiology **177**, 341–345 (1990).

[54]J. M. Boone, D. E. Pfeiffer, K. J. Strauss, R. P. Rossi, P. P. Lin, J. S. Shepard, and B. J. Conway, ''A survey of fluoroscopic exposure rates: AAPM task group No. 11 report,'' Med. Phys. **20**, 789–794 (1993).

[55]R. M. Gagne, C. N. West, R. F. Wagner, and P. W. Quinn, ''Laboratory measurements of sensitometry, MTF, veiling glare, Wiener spectrum and DQE for image intensifier tubes,'' Proc. SPIE **1896**, 248–258 (1993).

[56]H. Wieczorek, G. Frings, P. Quadflieg, and U. Schiebel, ''CsI:Tl for solid state x-ray detectors,'' Proceedings of the International Conference on Inorganic Scintillators and their Applications, Delft, Netherlands (1995).

[57]P. C. Bunch, K. E. Huff, and R. Van Metter, ''Analysis of the detective quantum efficiency of a radiographic screen-film combination,'' J. Opt. Soc. Am. A **4**, 902–909 (1987).

[58]R. Shaw, ''Quantifying the efficiency of imaging systems: A decade of progress in optimizing screen-films for x-ray detection,'' Proc. SPIE **2432**, 2–11 (1995).

[59]J. T. Dobbins, D. L. Ergun, L. Rutz, D. A. Hinshaw, H. Blume, and D. C. Clark, ''DQE(f) of four generations of computed radiography acquisition devices,'' Med. Phys. **22**, 1581–1593 (1995).

[60]P. M. de Groot, ''Image intensifier design and specifications,'' in Medical Physics Monograph No. 20, edited by J. A. Seibert, G. T. Barnes, and R. G. Gould, 429–460 (1994).

[61]R. M. Nishikawa and M. J. Yaffe, ''Signal-to-noise properties of mammographic film-screen systems,'' Med. Phys. **12**, 32–39 (1985).

[62]H. Roehrig, L. L. Fajardo, T. Yu, and W. S. Schempp, ''Signal, noise and detective quantum efficiency in CCD based x-ray imaging systems for use in mammography,'' Proc. SPIE **2163**, 320–332 (1994).

[63]R. A. Street, X. D. Wu, R. Weisfield, S. Ready, R. Apte, M. Nguyen, and P. Nylen, ''Two dimensional amorphous silicon image sensor arrays,'' Mater. Res. Soc. Symp. Proc. **377**, 757–766 (1995).

[64]L. E. Antonuk, J. Boudry, J. Yorkston, E. J. Morton, and W. Huang, ''Development of thin-film, flat-panel arrays for diagnostic and radiotherapy imaging,'' Proc. SPIE **1651**, 94–105 (1992).

[65]C. Van Berkel, N. C. Bird, C. J. Curling, and I. D. French, ''2D image sensor arrays with nip diodes,'' Mater. Res. Soc. Proc. **297**, 939–944 (1993).

[66]H. Mimura, K. Sai, Y. Ohta, K. Yamamoto, and K. Kitamura, ''A two-dimensional image sensor with a-Si:H pin diodes,'' Appl. Surf. Sci. **48/49**, 521–525 (1996).

[67]T. Graeve, W. Huang, S. M. Alexander, and Y. Li, ''Amorphous silicon image sensor for x-ray applications,'' Proc. SPIE **2415**, 177–181 (1995).

[68]M. Yamaguchi, Y. Kaneko, and K. Tsutsui, ''Two-dimensional contact-type image sensor using amorphous silicon photo-transistor,'' Jpn. J. Appl. Phys. **32**, 458–461 (1993).

[69]D. L. Lee, L. K. Cheung, and L. S. Jeromin, ''A new digital detector for projection radiography,'' Proc. SPIE **2432**, 237–249 (1995).